Progress In Electromagnetics Research, PIER 39, 1–45, 2003

TIME-DOMAIN EFIE, MFIE, AND CFIE FORMULATIONS USING LAGUERRE POLYNOMIALS AS TEMPORAL BASIS FUNCTIONS FOR THE ANALYSIS OF TRANSIENT SCATTERING FROM ARBITRARY SHAPED CONDUCTING STRUCTURES

B. H. Jung

Department of Information and Communication Engineering
Hoseo University
Asan, Chungnam 336-795, Korea

Y.-S. Chung

Department of Communication Engineering
Myongji University
Yongin, Kyunggi 449-728, Korea

T. K. Sarkar

Department of Electrical Engineering and Computer Science
Syracuse University
Syracuse, NY 13244-1240, USA

Abstract—In this paper, we present time-domain integral equation (TDIE) formulations for analyzing transient electromagnetic responses from three-dimensional (3-D) arbitrary shaped closed conducting bodies using the time-domain electric field integral equation (TD-EFIE), the time-domain magnetic field integral equation (TD-MFIE), and the time-domain combined field integral equation (TD-CFIE). Instead of the conventional marching-on in time (MOT) technique, the solution methods in this paper are based on the Galerkin's method that involves separate spatial and temporal testing procedure. Triangular patch basis functions are used for spatial expansion and testing functions for arbitrarily shaped 3-D structures. The time-domain unknown coefficient is approximated by using an orthonormal basis function set that is derived from the Laguerre functions. These basis functions are also used as temporal testing. Using these Laguerre functions it is possible to evaluate the time derivatives in an analytic

fashion. We also propose a second alternative formulation to solve the TDIE. The methods to be described result in very accurate and stable transient responses from conducting objects. Detailed mathematical steps are included and representative numerical results are presented and compared.

1. INTRODUCTION

The analysis of electromagnetic scattering from arbitrarily shaped conducting bodies in the frequency- and time-domain has been of considerable interest. In the analysis of closed conducting bodies, frequencies, which correspond to the internal resonance of the structure, may produce spurious solutions both for the electric field integral equation (EFIE) or for the magnetic field integral equation (MFIE). One possible way of obtaining a unique solution for closed objects at an internal resonant frequency is to combine the EFIE with MFIE in a linear function. This combination results in the combined field integral equation (CFIE). Although the CFIE formulation has been extensively used for conducting and dielectric bodies in the frequency-domain, only

a few researchers have applied it to the analysis of transient scattering by three-dimensional conducting bodies [1, 2].

For a TDIE solution, the MOT method is usually employed [3]. A serious drawback of this algorithm is the occurrence of late-time instabilities in the form of high frequency oscillations. Several MOT formulations have been presented for the solution of the TD-EFIE to calculate the electromagnetic scattering from arbitrary shaped 3-D structures using triangular patch modeling techniques. An explicit solution has been presented by differentiating the TD-EFIE and using second order finite difference [4]. But the results become unstable for late times. The late time oscillations could be eliminated by using an approximate average value of the current [5]. In addition, to overcome these late time instabilities, a backward finite difference approximation for the magnetic vector potential term has been presented for the explicit technique [6]. Recently an implicit scheme has been proposed to improve the stability problem [7, 8]. Even though employing the implicit technique, the stability and accuracy are dependent on the choice of the time step. A central finite difference methodology with the TD-EFIE is presented to improve the stability and the accuracy in [9] and [10]. The MOT scheme for the TD-MFIE is presented in [11], the results of which are more stable than those of the TD-EFIE. The solutions of the TD-CFIE with MOT scheme are presented and compared with solutions of the TD-EFIE and the TD-MFIE in [2]. This formulation eliminates the resonance problem that result in the late-time oscillation in the TD-EFIE and the slow varying oscillation in the TD-MFIE. However, solutions obtained using this scheme have still the instability and the accuracy is dependent on the size of the time step.

In this paper, we present a new technique to obtain stable responses of the TD-EFIE and the TD-MFIE for arbitrarily shaped 3-D conducting objects using Laguerre polynomials as temporal basis functions. Next, we combine the TD-EFIE and the TD-MFIE to obtain a matrix equation for the TD-CFIE. The Laguerre series are defined only over the interval from zero to infinity and, hence, are considered to be more suited for the transient problem, as they naturally enforce causality [12]. Using the Laguerre polynomials, we construct a set of orthonormal basis functions. Transient quantities that are functions of time can be spanned in terms of these orthogonal basis functions. The temporal basis functions used in this work are completely convergent to zero as time increases to infinity. Therefore, transient response spanned by these basis functions is also convergent to zero as time progresses. Using the Galerkin's method, we introduce a temporal testing procedure, which is similar to the spatial testing procedure

of the method of moments (MoM). By applying the temporal testing procedure to the TDIE, we can eliminate the numerical instabilities. Instead of the MOT procedure, we employ a marching-on in degree by increasing the degree of the temporal testing functions. Therefore, we can obtain the unknown coefficients by solving a matrix equation recursively with a finite number of basis functions. The minimum number of basis functions is dependent on the time duration and the frequency bandwidth product of an incident wave. We also propose an alternative formulation to solve the TD-EFIE, TD-MFIE, and TD-CFIE, respectively.

This paper is organized as follows. In the next section, we set up matrix equations by applying MoM with spatial and temporal testing procedure for the TD-EFIE, TD-MFIE, and TD-CFIE. In Section 3, alternative formulations are presented. In Section 4, we present and compare numerical results. Finally, some conclusions based on this work are discussed in Section 5.

2. FORMULATION

2.1. TD-EFIE

In this section we discuss the TD-EFIE and derive a matrix equation to obtain induced currents on the conducting scatterer. Let S denote the surface of a closed or open conducting body illuminated by a transient electromagnetic wave. Since the total tangential electric field is zero on the surface for all times, we have

$$\left[\mathbf{E}^i(\mathbf{r},t)+\mathbf{E}^s(\mathbf{r},t)\right]_{\tan}=0, \quad \mathbf{r}\in S \tag{1}$$

where $\mathbf{E}^i$ is the incident field and $\mathbf{E}^s$ is the scattered field due to the induced current $\mathbf{J}$. The subscript 'tan' denotes the tangential component. The scattered field is given by

$$\mathbf{E}^s(\mathbf{r},t)=-\frac{\partial}{\partial t}\mathbf{A}(\mathbf{r},t)-\nabla\Phi(\mathbf{r},t). \tag{2}$$

The expressions for $\mathbf{A}$ and Φ, which represent the magnetic vector and electric scalar potentials, respectively, can be written as

$$\mathbf{A}(\mathbf{r},t)=\frac{\mu}{4\pi}\int_S\frac{\mathbf{J}(\mathbf{r}',\tau)}{R}dS' \tag{3}$$

$$\Phi(\mathbf{r},t)=\frac{1}{4\pi\varepsilon}\int_S\frac{q(\mathbf{r}',\tau)}{R}dS'. \tag{4}$$

In (3) and (4), $R = |\mathbf{r} - \mathbf{r}'|$ represents the distance between the arbitrarily located observation point $\mathbf{r}$ and the source point $\mathbf{r}'$. $\tau = t - R/c$ is the retarded time. μ and ε are the permeability and the permittivity of the medium, and c is the velocity of the propagation of the electromagnetic wave in that space. The surface charge density q is related to the surface current density $\mathbf{J}$ by the equation of continuity

$$\nabla \cdot \mathbf{J}(\mathbf{r}, t) = -\frac{\partial}{\partial t} q(\mathbf{r}, t). \tag{5}$$

Combining (1) and (2) gives

$$\left[\frac{\partial}{\partial t}\mathbf{A}(\mathbf{r}, t) + \nabla\Phi(\mathbf{r}, t)\right]_{\tan} = \left[\mathbf{E}^i(\mathbf{r}, t)\right]_{\tan}, \quad \mathbf{r} \in S. \tag{6}$$

Equation (6) in conjunction with (3) and (4) constitutes a TD-EFIE, from which the unknown current $\mathbf{J}$ may be determined.

The surface of the structure to be analyzed is approximated by planar triangular patches. As in [13], we define the spatial basis function associated with the n^{th} common edge as

$$\mathbf{f}_n(\mathbf{r}) = \mathbf{f}_n^+(\mathbf{r}) + \mathbf{f}_n^-(\mathbf{r}) \tag{7a}$$

$$\mathbf{f}_n^{\pm}(\mathbf{r}) = \begin{cases} \dfrac{l_n}{2A_n^{\pm}}\boldsymbol{\rho}_n^{\pm}, & \mathbf{r} \in T_n^{\pm} \\ 0, & \mathbf{r} \notin T_n^{\pm} \end{cases} \tag{7b}$$

where l_n and $A_n^{\pm}$ are the length of the edge and the area of triangle $T_n^{\pm}$. $\boldsymbol{\rho}_n^{\pm}$ is the position vector defined with respect to the free vertex of $T_n^{\pm}$. The electric current $\mathbf{J}$ on the scattering structure may be approximated in terms of the vector basis function as

$$\mathbf{J}(\mathbf{r}, t) = \sum_{n=1}^{N} J_n(t)\mathbf{f}_n(\mathbf{r}) \tag{8}$$

where N represents the number of common edges, discounting the boundary edges in the triangulated model of the conducting object. When (8) is used in (6), we encounter a time integral term from equations (4) and (5). To avoid this problem and to handle the time derivative of the vector potential analytically, we introduce a new source vector $\mathbf{e}(\mathbf{r}, t)$ defined by

$$\mathbf{J}(\mathbf{r}, t) = \frac{\partial}{\partial t}\mathbf{e}(\mathbf{r}, t) \tag{9}$$

where the relation between this source vector and charge density is given through

$$q(\mathbf{r},t) = -\nabla \cdot \mathbf{e}(\mathbf{r},t). \tag{10}$$

By using (8) and (9), we may express

$$\mathbf{e}(\mathbf{r},t) = \sum_{n=1}^{N} e_n(t)\mathbf{f}_n(\mathbf{r}). \tag{11}$$

We now solve (6) by applying Galerkin's method in the MoM context and hence the testing functions are same as the expansion functions. By choosing the spatial expansion function $\mathbf{f}_m(\mathbf{r})$ also as the spatial testing functions, we have from (6)

$$\left\langle \mathbf{f}_m(\mathbf{r}), \frac{\partial}{\partial t}\mathbf{A}(\mathbf{r},t)\right\rangle + \left\langle \mathbf{f}_m(\mathbf{r}), \nabla\Phi(\mathbf{r},t)\right\rangle = \left\langle \mathbf{f}_m(\mathbf{r}), \mathbf{E}^i(\mathbf{r},t)\right\rangle \tag{12}$$

where $m = 1, 2, \ldots, N$. The next step in the MoM procedure is to substitute the unknown expansion functions defined in (11) with (9) into (12). First, we consider the testing integral of the magnetic vector potential. Using (3), (9), and (11), we have

$$\left\langle \mathbf{f}_m(\mathbf{r}), \frac{\partial}{\partial t}\mathbf{A}(\mathbf{r},t)\right\rangle = \sum_{n=1}^{N} \frac{\mu}{4\pi}\int_S \mathbf{f}_m(\mathbf{r}) \cdot \int_S \frac{d^2}{dt^2} e_n(\tau)\frac{\mathbf{f}_n(\mathbf{r}')}{R} dS' dS. \tag{13}$$

In computing the integral in (13), we assume that the unknown transient quantity does not change appreciably within the triangle so that

$$\tau = t - \frac{R}{c} \quad \rightarrow \quad \tau_{mn}^{pq} = t - \frac{R_{mn}^{pq}}{c}, \quad R_{mn}^{pq} = |\mathbf{r}_m^{cp} - \mathbf{r}_n^{cq}| \tag{14}$$

where p and q are $+$ or $-$. $\mathbf{r}_m^{c\pm}$ is the position vector of the center in triangle $T_n^{\pm}$. With the assumption (14), (13) can be written as

$$\left\langle \mathbf{f}_m(\mathbf{r}), \frac{\partial}{\partial t}\mathbf{A}(\mathbf{r},t)\right\rangle = \sum_{n=1}^{N}\sum_{p,q} \mu a_{mn}^{pq} \frac{d^2}{dt^2} e_n(\tau_{mn}^{pq}) \tag{15}$$

where

$$a_{mn}^{pq} = \frac{1}{4\pi}\int_S \mathbf{f}_m^p(\mathbf{r}) \cdot \int_S \frac{\mathbf{f}_n^q(\mathbf{r}')}{R} dS' dS. \tag{16}$$

Next, we consider the testing of the gradient of the scalar potential in (12). Using the vector identity $\nabla \cdot \phi \mathbf{A} = \mathbf{A} \cdot \nabla\phi + \phi\nabla \cdot \mathbf{A}$ and the property of the spatial basis function [13], we can write

$$\begin{aligned}\left\langle \mathbf{f}_m(\mathbf{r}), \nabla\Phi(\mathbf{r},t)\right\rangle &= -\int_S \nabla\cdot\mathbf{f}_m(\mathbf{r})\Phi(\mathbf{r},t)dS \\ &= \sum_{n=1}^{N}\frac{1}{4\pi\varepsilon}\int_S \nabla\cdot\mathbf{f}_m(\mathbf{r})\int_S e_n(\tau)\frac{\nabla'\cdot\mathbf{f}_n(\mathbf{r}')}{R}dS'dS.\end{aligned} \tag{17}$$

With the assumption (14), (17) can be written as

$$\left\langle \mathbf{f}_m(\mathbf{r}), \nabla\Phi(\mathbf{r},t)\right\rangle = \sum_{n=1}^{N}\sum_{p,q}\frac{b_{mn}^{pq}}{\varepsilon}e_n(\tau_{mn}^{pq}) \tag{18}$$

where

$$b_{mn}^{pq} = \frac{1}{4\pi}\int_S \nabla\cdot\mathbf{f}_m^p(\mathbf{r})\int_S \frac{\nabla'\cdot\mathbf{f}_n^q(\mathbf{r}')}{R}dS'dS. \tag{19}$$

Substituting (15) and (18) into (12), we obtain

$$\sum_{n=1}^{N}\sum_{p,q}\left[\mu a_{mn}^{pq}\frac{d^2}{dt^2}e_n(\tau_{mn}^{pq}) + \frac{b_{mn}^{pq}}{\varepsilon}e_n(\tau_{mn}^{pq})\right] = V_m^E(t) \tag{20}$$

where

$$V_m^E(t) = \int_S \mathbf{f}_m(\mathbf{r})\cdot\mathbf{E}^i(\mathbf{r},t)dS. \tag{21}$$

The integrals (16), (19), and (21) may be evaluated by the method described in [13] and [14].

Now, we consider the temporal expansion and testing procedures. An orthonormal basis function set can be derived from the Laguerre functions through the representation [12]

$$\phi_j(t) = e^{-t/2}L_j(t) \tag{22}$$

where $L_j(t)$ is the Laguerre polynomial of degree j. The various mathematical properties of this function are introduced in the Appendix. These functions can approximate a causal response quite well. The transient coefficient introduced in (11) can be expanded as

$$e_n(t) = \sum_{j=0}^{\infty} e_{n,j}\phi_j(st) \tag{23}$$

where s is a scaling factor. By controlling this factor s, the support provided by the expansion can be increased or decreased. Using (A9) and (A10) in the Appendix, therefore, the expressions of expanding the first and the second derivative of the transient coefficient are given as, respectively,

$$\frac{d}{dt}e_n(t) = s\sum_{j=0}^{\infty}\left[\frac{1}{2}e_{n,j} + \sum_{k=0}^{j-1}e_{n,k}\right]\phi_j(st) \tag{24}$$

$$\frac{d^2}{dt^2}e_n(t) = s^2\sum_{j=0}^{\infty}\left[\frac{1}{4}e_{n,j} + \sum_{k=0}^{j-1}(j-k)e_{n,k}\right]\phi_j(st). \tag{25}$$

Substituting (23) and (25) into (20) and taking a temporal testing with $\phi_i(st)$, which is the Laguerre transform defined in (A7) in the Appendix, we have

$$\sum_{n=1}^{N}\sum_{p,q}\sum_{j=0}^{\infty}\left[\left(\frac{s^2}{4}\mu a_{mn}^{pq} + \frac{b_{mn}^{pq}}{\varepsilon}\right)e_{n,j} + s^2\mu a_{mn}^{pq}\sum_{k=0}^{j-1}(j-k)e_{n,k}\right] \cdot I_{ij}\left(s\frac{R_{mn}^{pq}}{c}\right) = V_{m,i}^{E} \tag{26}$$

where

$$I_{ij}\left(s\frac{R_{mn}^{pq}}{c}\right) = \int_0^{\infty}\phi_i(st)\phi_j\left(st - s\frac{R_{mn}^{pq}}{c}\right)d(st) \tag{27}$$

$$V_{m,i}^{E} = \int_0^{\infty}\phi_i(st)V_m^E(t)d(st). \tag{28}$$

The evaluation of the integral (27) is explained in the Appendix. We note that $I_{ij} = 0$ when $j > 1$ from (A15) in the Appendix. Therefore we can write the upper limit of the third summation symbol as i instead of ∞ in (26). In this result, moving the terms including $e_{n,j}$, which is known for $j < i$, to the right-hand side, we obtain

$$\begin{aligned}\sum_{n=1}^{N}\sum_{p,q}\left(\frac{s^2}{4}\mu a_{mn}^{pq} + \frac{b_{mn}^{pq}}{\varepsilon}\right)e_{n,i}I_{ii}\left(s\frac{R_{mn}^{pq}}{c}\right) &= V_{m,i}^{E} - \sum_{n=1}^{N}\sum_{p,q}\sum_{j=0}^{i-1}\left(\frac{s^2}{4}\mu a_{mn}^{pq} + \frac{b_{mn}^{pq}}{\varepsilon}\right)e_{n,j}I_{ij}\left(s\frac{R_{mn}^{pq}}{c}\right) \\ &\quad - \sum_{n=1}^{N}\sum_{p,q}\sum_{j=0}^{i}s^2\mu a_{mn}^{pq}\sum_{k=0}^{j-1}(j-k)e_{n,k}I_{ij}\left(s\frac{R_{mn}^{pq}}{c}\right).\end{aligned} \tag{29}$$

Rewriting (29) in a simple form, we have

$$\sum_{n=1}^{N} \alpha_{mn}^{E} e_{n,i} = V_{m,i}^{E} + P_{m,i}^{E} \tag{30}$$

where

$$\alpha_{mn}^{E} = \sum_{p,q} \left(\frac{s^2}{4} \mu a_{mn}^{pq} + \frac{b_{mn}^{pq}}{\varepsilon} \right) \exp\left(-s \frac{R_{mn}^{pq}}{2c} \right) \tag{31}$$

$$P_{m,i}^{E} = -\sum_{n=1}^{N} \sum_{p,q} \left[\left(\frac{s^2}{4} \mu a_{mn}^{pq} + \frac{b_{mn}^{pq}}{\varepsilon} \right) \sum_{j=0}^{i-1} e_{n,j} I_{ij} \left(s \frac{R_{mn}^{pq}}{c} \right) + s^2 \mu a_{mn}^{pq} \sum_{j=0}^{i} \sum_{k=0}^{j-1} (j-k) e_{n,k} I_{ij} \left(s \frac{R_{mn}^{pq}}{c} \right) \right]. \tag{32}$$

In obtaining (31), we used $I_{ii}(y) = e^{-y/2}$ from (A15). Finally, we can write (30) in a matrix form as

$$\left[\alpha_{mn}^{E}\right] \left[e_{n,i}\right] = \left[\gamma_{m,i}^{E}\right] \tag{33}$$

where $\gamma_{m,i}^{E} = V_{m,i}^{E} + P_{m,i}^{E}$ and $i = 0, 1, \ldots, \infty$. It is important to note that $\left[\alpha_{mn}^{E}\right]$ is not a function of the degree of the temporal testing function. Therefore, we can obtain the unknown coefficients by solving (33) as increasing the degree of the temporal testing functions.

2.2. TD-MFIE

We can also develop the TD-MFIE that uses the boundary condition for the magnetic field. Let S represent the surface of a closed conducting body illuminated by a transient electromagnetic plane wave. From the boundary conditions, we obtain

$$\mathbf{n} \times \left[\mathbf{H}^{i}(\mathbf{r}, t) + \mathbf{H}^{s}(\mathbf{r}, t) \right] = \mathbf{J}(\mathbf{r}, t), \quad \mathbf{r} \in S \tag{34}$$

where $\mathbf{n}$ represents an outward-directed unit vector normal to the surface S at a field point. $\mathbf{H}^{i}$ is the incident field, and $\mathbf{H}^{s}$ is the scattered magnetic field due to the induced currents $\mathbf{J}$. The scattered magnetic field can be written in terms of the potential functions, and is given by

$$\mathbf{H}^{s}(\mathbf{r}, t) = \frac{1}{\mu} \nabla \times \mathbf{A}(\mathbf{r}, t) \tag{35}$$

where the magnetic vector potential $\mathbf{A}$ is given in (3). We note that (34) along with (35) represents the TD-MFIE. Extracting the Cauchy principal value from the curl term, we may write (35) as

$$\mathbf{n} \times \mathbf{H}^s(\mathbf{r}, t) = \frac{\mathbf{J}(\mathbf{r}, t)}{2} + \mathbf{n} \times \frac{1}{4\pi} \int_{S_0} \nabla \times \frac{\mathbf{J}(\mathbf{r}', \tau)}{R} dS' \tag{36}$$

where S_0 denotes the surface with the contribution due to the singularity at $\mathbf{r} = \mathbf{r}'$ or $R = 0$, removed from the surface S. Now, by substituting (36) into (34), we obtain

$$\frac{\mathbf{J}(\mathbf{r}, t)}{2} - \mathbf{n} \times \frac{1}{4\pi} \int_{S_0} \nabla \times \frac{\mathbf{J}(\mathbf{r}', \tau)}{R} dS' = \mathbf{n} \times \mathbf{H}^i(\mathbf{r}, t). \tag{37}$$

Applying the spatial testing procedure to (37), we get

$$\left\langle \mathbf{f}_m(\mathbf{r}), \frac{\mathbf{J}(\mathbf{r}, t)}{2} \right\rangle - \left\langle \mathbf{f}_m(\mathbf{r}), \mathbf{n} \times \frac{1}{4\pi} \int_{S_0} \nabla \times \frac{\mathbf{J}(\mathbf{r}', \tau)}{R} dS' \right\rangle = \left\langle \mathbf{f}_m(\mathbf{r}), \mathbf{n} \times \mathbf{H}^i(\mathbf{r}, t) \right\rangle \tag{38}$$

Now, we consider the inner product integrals in (38). Substitution of (9) and (11) into (38), the first term of (38) becomes

$$\left\langle \mathbf{f}_m(\mathbf{r}), \frac{\mathbf{J}(\mathbf{r}, t)}{2} \right\rangle = \sum_{n=1}^{N} c_{mn} \frac{d}{dt} e_n(t) \tag{39}$$

where

$$c_{mn} = c_{mn}^{++} + c_{mn}^{+-} + c_{mn}^{-+} + c_{mn}^{--} = \sum_{p,q} c_{mn}^{pq} \tag{40}$$

$$c_{mn}^{pq} = \frac{1}{2} \int_S \mathbf{f}_m^p(\mathbf{r}) \cdot \mathbf{f}_n^q(\mathbf{r}) dS. \tag{41}$$

The integral of (41) can be computed analytically and the result is given by [15]. The curl operator inside the integral in the second term of (38) is given by [16]

$$\nabla \times \frac{\mathbf{J}(\mathbf{r}', \tau)}{R} = \frac{1}{c} \frac{\partial}{\partial t} \mathbf{J}(\mathbf{r}', \tau) \times \frac{\widehat{\mathbf{R}}}{R} + \mathbf{J}(\mathbf{r}', \tau) \times \frac{\widehat{\mathbf{R}}}{R^2} \tag{42}$$

where $\widehat{\mathbf{R}}$ is a unit vector along the direction $\mathbf{r}-\mathbf{r}'$. Thus, using (42), the second term in (38) becomes

$$\begin{aligned}\Big\langle \mathbf{f}_m(\mathbf{r}), \mathbf{n}\times\frac{1}{4\pi}\int_{S_0}\nabla\times\frac{\mathbf{J}(\mathbf{r}',\tau)}{R}dS'\Big\rangle \\ = \sum_{n=1}^{N}\frac{1}{4\pi}\int_S \mathbf{f}_m(\mathbf{r})\cdot\mathbf{n}\times\int_{S_0}\Big[\frac{1}{c}\frac{d^2}{dt^2}e_n(\tau)\mathbf{f}_n(\mathbf{r}')\times\frac{\widehat{\mathbf{R}}}{R} \\ + \frac{d}{dt}e_n(\tau)\mathbf{f}_n(\mathbf{r}')\times\frac{\widehat{\mathbf{R}}}{R^2}\Big]dS'dS. \end{aligned} \tag{43}$$

Assume that the retarded time can be written as in (14), we obtain

$$\begin{aligned}\Big\langle \mathbf{f}_m(\mathbf{r}), \mathbf{n}\times\frac{1}{4\pi}\int_{S_0}\nabla\times\frac{\mathbf{J}(\mathbf{r}',\tau)}{R}dS'\Big\rangle \\ = \sum_{n=1}^{N}\sum_{p,q}\Big[\frac{I_1^{pq}}{c}\frac{d^2}{dt^2}e_n(\tau_{mn}^{pq}) + I_2^{pq}\frac{d}{dt}e_n(\tau_{mn}^{pq})\Big] \end{aligned} \tag{44}$$

where

$$I_v^{pq} = \frac{1}{4\pi}\int_S \mathbf{f}_m^p(\mathbf{r})\cdot\mathbf{n}\times\int_S \mathbf{f}_n^q(\mathbf{r}')\times\frac{\widehat{\mathbf{R}}}{R^v}dS'dS, \quad v=1,2. \tag{45}$$

Substituting (39) and (44) into (38), we obtain

$$\sum_{n=1}^{N}\Big[c_{mn}\frac{d}{dt}e_n(t) - \sum_{p,q}\Big\{\frac{I_1^{pq}}{c}\frac{d^2}{dt^2}e_n(\tau_{mn}^{pq}) + I_2^{pq}\frac{d}{dt}e_n(\tau_{mn}^{pq})\Big\}\Big] = V_m^H(t) \tag{46}$$

where

$$V_m^H(t) = \int_S \mathbf{f}_m(\mathbf{r})\cdot\mathbf{n}\times\mathbf{H}^i(\mathbf{r},t)dS. \tag{47}$$

The integral (45) and (47) may be evaluated using the Gaussian quadrature scheme for unprimed and primed coordinates numerically.

Substituting (24) and (25) into (46) and taking a temporal testing

with respect to $\phi_i(st)$, we obtain

$$\sum_{n=1}^{N}\Bigg[sc_{mn}\sum_{j=0}^{\infty}\left(\frac{1}{2}e_{n,j}+\sum_{k=0}^{j-1}e_{n,k}\right)\delta_{ij} - \sum_{p,q}\Bigg\{s^2\frac{I_1^{pq}}{c}\sum_{j=0}^{\infty}\left(\frac{1}{4}e_{n,j}+\sum_{j=0}^{j-1}(j-k)e_{n,k}\right)I_{ij}\left(s\frac{R_{mn}^{pq}}{c}\right) + sI_2^{pq}\sum_{j=0}^{\infty}\left(\frac{e_{n,j}}{2}+\sum_{k=0}^{j-1}e_{n,k}\right)I_{ij}\left(s\frac{R_{mn}^{pq}}{c}\right)\Bigg\}\Bigg] = V_{m,i}^{H} \quad (48)$$

where I_{ij} is given in (27), and

$$V_{m,i}^{H} = \int_0^{\infty}\phi_i(st)V_m^H(t)d(st). \quad (49)$$

Because $I_{ij}=0$ when $j>i$ from (A15), we can write the upper limit in the summation symbol as i instead of ∞ in (48). In this result, moving the terms including $e_{n,j}$, which is known for $j<i$, to the right-hand side, we obtain

$$\sum_{n=1}^{N}\left\{\frac{s}{2}c_{mn}e_{n,i}-\sum_{p,q}\left(\frac{s^2}{4}\frac{I_1^{pq}}{c}+\frac{s}{2}I_2^{pq}\right)e_{n,i}I_{ii}\left(s\frac{R_{mn}^{pq}}{c}\right)\right\} = V_{m,i} - \sum_{n=1}^{N}\Bigg[sc_{mn}\sum_{k=0}^{i-1}e_{n,k} - \sum_{p,q}\Bigg\{\sum_{j=0}^{i}\sum_{k=0}^{j-1}\left(s^2\frac{I_1^{pq}}{c}(j-k)+sI_2^{pq}\right) \cdot e_{n,k}I_{ij}\left(s\frac{R_{mn}^{pq}}{c}\right)+\sum_{j=0}^{i-1}\left(\frac{s^2}{4}\frac{I_1^{pq}}{c}+\frac{s}{2}I_2^{pq}\right)e_{n,j}I_{ij}\left(s\frac{R_{mn}^{pq}}{c}\right)\Bigg\}\Bigg] \quad (50)$$

Rewriting (50) in a simple form, we obtain

$$\sum_{n=1}^{N}\alpha_{mn}^{H}e_{n,i} = V_{m,i}^{H}+P_{m,i}^{H} \quad (51)$$

where

$$\alpha_{mn}^{H} = \frac{s}{2}c_{mn}-\sum_{p,q}\left(\frac{s^2}{4}\frac{I_1^{pq}}{c}+\frac{s}{2}I_2^{pq}\right)\exp\left(-s\frac{R_{mn}^{pq}}{2c}\right) \quad (52)$$

$$P_{m,i}^{H} = -\sum_{n=1}^{N}\Bigg[sc_{mn}\sum_{k=0}^{i-1}e_{n,k} - \sum_{p,q}\Bigg\{\left(\frac{s^2}{4}\frac{I_1^{pq}}{c} + \frac{s}{2}I_2^{pq}\right) \cdot \sum_{j=0}^{i-1} e_{n,j} I_{ij}\left(s\frac{R_{mn}^{pq}}{c}\right) + s^2\frac{I_1^{pq}}{c}\sum_{j=0}^{i}\sum_{k=0}^{i-1}(j-k)e_{n,k}I_{ij}\left(s\frac{R_{mn}^{pq}}{c}\right) + sI_2^{pq}\sum_{j=0}^{i}\sum_{k=0}^{j-1}e_{n,k}I_{ij}\left(s\frac{R_{mn}^{pq}}{c}\right)\Bigg\}\Bigg]. \tag{53}$$

We can write (51) in a matrix form as

$$\left[\alpha_{mn}^{H}\right]\left[e_{n,i}\right] = \left[\gamma_{m,i}^{H}\right] \tag{54}$$

where $\gamma_{m,i}^{H} = V_{m,i}^{H} + P_{m,i}^{H}$ and $i = 0, 1, \ldots, \infty$.

2.3. TD-CFIE

The TD-CFIE is obtained by means of a linear combination of the TD-EFIE with the TD-MFIE [17] through

$$(1-\kappa)[-\mathbf{E}^s(\mathbf{r},t)]_{\tan} + \kappa\eta[\mathbf{J} - \hat{n}\times\mathbf{H}^s(\mathbf{r},t)] = (1-\kappa)[\mathbf{E}^i(\mathbf{r},t)]_{\tan} + \kappa\eta[\hat{n}\times\mathbf{H}^i(\mathbf{r},t)] \tag{55}$$

where κ is the parameter of the linear combination, which is between 0 (EFIE) and 1 (MFIE), and η is the wave impedance of the space. We obtain a matrix equation for the TD-CFIE directly from (33) and (54) as

$$\left[\alpha_{mn}\right]\left[e_{n,i}\right] = \left[\gamma_{m,i}\right], \quad i = 0, 1, \ldots, \infty \tag{56}$$

$$\alpha_{mn} = \kappa\alpha_{mn}^{E} + \eta(1-\kappa)\alpha_{mn}^{H} \tag{57}$$

$$\gamma_{m,i} = \kappa\gamma_{m,i}^{E} + \eta(1-\kappa)\gamma_{m,i}^{H} \tag{58}$$

We need the minimum number of temporal basis functions, M, in computing (56). This parameter is dependent on the time duration of the transient response and the bandwidth of the excitation signal. We consider a signal with a bandwidth B in the frequency domain and of time duration T_f. When we represent this signal by a Fourier series, the range of the sampling frequency is $-B \le k\Delta f \le B$, where k is an integer and $\Delta f = 1/T_f$. So we get $|k| \le B/T_f$. Hence the minimum number of temporal basis functions becomes $M = 2BT_f + 1$. We note that the upper limit of the integral in (28) and (49) can be replaced by the time duration T_f instead of infinity.

2.4. Current and Far Field

By solving the matrix equation (56) in a marching-on in degree manner with M temporal basis functions, the electric transient current coefficient in (8) is expressed using the relation (9) and (11) with (24) as

$$J_n(t) = \frac{d}{dt} e_n(t) = s \sum_{j=0}^{M-1} \left(\frac{1}{2} e_{n,j} + \sum_{k=0}^{j-1} e_{n,k} \right) \phi_j(st). \tag{59}$$

Once the current coefficients have been obtained, we can compute the far field anywhere. We explain the analytic method to compute the far field directly by using the coefficient $e_n(t)$ obtained from (56). Neglecting the scalar potential term, the far field is given by

$$\mathbf{E}^s(\mathbf{r}, t) \approx -\frac{\partial}{\partial t} \mathbf{A}(\mathbf{r}, t). \tag{60}$$

Substituting (3), (9), and (11) into (60) with (7a), we get

$$\mathbf{E}^s(\mathbf{r}, t) \approx -\frac{\mu}{4\pi} \sum_{n=1}^{N} \sum_{q} \int_S \frac{d^2}{dt^2} e_n(\tau) \frac{\mathbf{f}_n^q(\mathbf{r}')}{R} dS'. \tag{61}$$

We make the following approximation in the far field:

$$\begin{array}{ll} R \approx r - \mathbf{r}' \cdot \hat{\mathbf{r}} & \text{for the time retardation term } t - R/c \\ R \approx r & \text{for the amplitude term } 1/R \end{array}$$

where $\hat{\mathbf{r}} = \mathbf{r}/r$ is a unit vector in the direction of the radiation. The integral in (61) is evaluated by approximating the integrand by the value at the center of the source triangle T_n^q. Substituting (7b) into (61) and approximating $\mathbf{r}' \approx \mathbf{r}_n^{cq}$ and $\boldsymbol{\rho}_n^q \approx \boldsymbol{\rho}_n^{cq}$, we obtain

$$\mathbf{E}^s(\mathbf{r}, t) \approx -\frac{\mu}{8\pi r} \sum_{n=1}^{N} l_n \sum_{q} \boldsymbol{\rho}_n^{cq} \frac{d^2}{dt^2} e_n(\tau_n^q) \tag{62}$$

where $\tau_n^q \approx t - (r - \mathbf{r}_n^{cq} \cdot \hat{\mathbf{r}})/c$ and

$$\frac{d^2}{dt^2} e_n(\tau_n^q) = s^2 \sum_{j=0}^{M-1} \left[\frac{1}{4} e_{n,j} + \sum_{k=0}^{j-1} (j-k) e_{n,k} \right] \phi_j(s\tau_n^q). \tag{63}$$

3. AN ALTERNATIVE FORMULATION

3.1. TD-EFIE

In this section, we present an alternative method for solving TD-EFIE given in (1). By differentiating (6), we get

$$\left[\frac{\partial^2}{\partial t^2}\mathbf{A}(\mathbf{r},t)+\nabla\frac{\partial}{\partial t}\Phi(\mathbf{r},t)\right]_{\tan}=\left[\frac{\partial}{\partial t}\mathbf{E}^i(\mathbf{r},t)\right]_{\tan},\quad \mathbf{r}\in S. \tag{64}$$

Using a similar procedure in obtaining (12), we get the result of the spatial testing from (64) as

$$\left\langle \mathbf{f}_m(\mathbf{r}),\frac{\partial^2}{\partial t^2}\mathbf{A}(\mathbf{r},t)\right\rangle+\left\langle \mathbf{f}_m(\mathbf{r}),\nabla\frac{\partial}{\partial t}\Phi(\mathbf{r},t)\right\rangle=\left\langle \mathbf{f}_m(\mathbf{r}),\frac{\partial}{\partial t}\mathbf{E}^i(\mathbf{r},t)\right\rangle. \tag{65}$$

Substituting (3)–(5), (7), and (8) into (65) with the assumption (14), we get

$$\sum_{n=1}^{N}\sum_{p,q}\left[\mu a_{mn}^{pq}\frac{d^2}{dt^2}J_n(\tau_{mn}^{pq})+\frac{b_{mn}^{pq}}{\varepsilon}J_n(\tau_{mn}^{pq})\right]=V_m^E(t) \tag{66}$$

where a_{mn}^{pq} and b_{mn}^{pq} have been defined in (16) and (19), respectively, and

$$V_m^E(t)=\int_S \mathbf{f}_m(\mathbf{r})\cdot\frac{\partial}{\partial t}\mathbf{E}^i(\mathbf{r},t)dS. \tag{67}$$

The transient current can be written as

$$J_n(t)=\sum_{j=0}^{\infty}J_{n,j}\phi_j(st) \tag{68}$$

where s is a scaling factor. Using (A9) and (A10) in the Appendix, the first and the second derivatives of the transient current are given as

$$\frac{d}{dt}J_n(t)=s\sum_{j=0}^{\infty}\left[\frac{1}{2}J_{n,j}+\sum_{k=0}^{j-1}J_{n,k}\right]\phi_j(st) \tag{69}$$

$$\frac{d^2}{dt^2}J_n(t)=s^2\sum_{j=0}^{\infty}\left[\frac{1}{4}J_{n,j}+\sum_{k=0}^{j-1}(j-k)J_{n,k}\right]\phi_j(st). \tag{70}$$

Substituting (68) and (70) into (66) and performing the temporal testing with $\phi_i(st)$, we get

$$\sum_{n=1}^{N}\sum_{p,q}\sum_{j=0}^{\infty}\left[\left(\frac{s^2}{4}\mu a_{mn}^{pq}+\frac{b_{mn}^{pq}}{\varepsilon}\right)J_{n,j}+s^2\mu a_{mn}^{pq}\sum_{k=0}^{j-1}(j-k)J_{n,k}\right] \cdot I_{ij}\left(s\frac{R_{mn}^{pq}}{c}\right)=V_{m,i}^{E} \quad (71)$$

where $V_{m,i}^{E}$ is of the same form given in (28), but $V_m^E(t)$ is given by (67). Changing the upper limit of the summation symbol to i instead of ∞ in (71) and moving the terms including $J_{n,j}$, which is known for $j<i$, to the right-hand side, we obtain

$$\begin{aligned}\sum_{n=1}^{N}\sum_{p,q}\left(\frac{s^2}{4}\mu a_{mn}^{pq}+\frac{b_{mn}^{pq}}{\varepsilon}\right)J_{n,i}I_{ii}\left(s\frac{R_{mn}^{pq}}{c}\right)&=V_{m,i}^{E}-\sum_{n=1}^{N}\sum_{p,q}\sum_{j=0}^{i-1}\left(\frac{s^2}{4}\mu a_{mn}^{pq}+\frac{b_{mn}^{pq}}{\varepsilon}\right)J_{n,j}I_{ij}\left(s\frac{R_{mn}^{pq}}{c}\right)\\&\quad-\sum_{n=1}^{N}\sum_{p,q}\sum_{j=0}^{i}s^2\mu a_{mn}^{pq}\sum_{k=0}^{j-1}(j-k)J_{n,k}I_{ij}\left(s\frac{R_{mn}^{pq}}{c}\right). \quad (72)\end{aligned}$$

Rewriting (72) in a simple form, we have

$$\sum_{n=1}^{N}\alpha_{mn}^{E}J_{n,i}=V_{m,i}^{E}+P_{m,i}^{E} \quad (73)$$

where α_{mn}^{E} is defined in (31) and

$$\begin{aligned}P_{m,i}^{E}=-\sum_{n=1}^{N}\sum_{p,q}\Bigg[&\left(\frac{s^2}{4}\mu a_{mn}^{pq}+\frac{b_{mn}^{pq}}{\varepsilon}\right)\sum_{j=0}^{i-1}J_{n,j}I_{ij}\left(s\frac{R_{mn}^{pq}}{c}\right)\\&+s^2\mu a_{mn}^{pq}\sum_{j=0}^{i}\sum_{k=0}^{j-1}(j-k)J_{n,k}I_{ij}\left(s\frac{R_{mn}^{pq}}{c}\right)\Bigg]. \quad (74)\end{aligned}$$

Lastly, we can write (73) in a matrix form as

$$\left[\alpha_{mn}^{E}\right]\left[J_{n,i}\right]=\left[\gamma_{m,i}^{E}\right] \quad (75)$$

where $\gamma_{m,i}^{E}=V_{m,i}^{E}+P_{m,i}^{E}$ and $i=0,1,\ldots,\infty$.

3.2. TD-MFIE

To combine the TD-MFIE with the TD-EFIE developed in the previous section, we introduce an alternative procedure to set up a matrix equation for the TD-MFIE. Using the transient current coefficient expansion (8), we obtain the result of the inner product for the first term in (38) as

$$\left\langle \mathbf{f}_m(\mathbf{r}), \frac{\mathbf{J}(\mathbf{r},t)}{2} \right\rangle = \sum_{n=1}^{N} c_{mn} J_n(t) \tag{76}$$

where c_{mn} is same as (40). Similarly, using (8) and (42) we obtain the result for the second term in (38) as

$$\begin{aligned} &\left\langle \mathbf{f}_m(\mathbf{r}), \mathbf{n} \times \frac{1}{4\pi} \int_{S_0} \nabla \times \frac{\mathbf{J}(\mathbf{r}',\tau)}{R} dS' \right\rangle \\ &= \sum_{n=1}^{N} \frac{1}{4\pi} \int_S \mathbf{f}_m(\mathbf{r}) \cdot \mathbf{n} \times \int_{S_0} \left[\frac{1}{c} \frac{d}{dt} J_n(\tau) \mathbf{f}_n(\mathbf{r}') \times \frac{\widehat{\mathbf{R}}}{R} + J_n(\tau) \mathbf{f}_n(\mathbf{r}') \times \frac{\widehat{\mathbf{R}}}{R^2} \right] dS' dS. \end{aligned} \tag{77}$$

Using (14), we obtain

$$\begin{aligned} &\left\langle \mathbf{f}_m(\mathbf{r}), \mathbf{n} \times \frac{1}{4\pi} \int_{S_0} \nabla \times \frac{\mathbf{J}(\mathbf{r}',\tau)}{R} dS' \right\rangle \\ &\qquad = \sum_{n=1}^{N} \sum_{p,q} \left[\frac{I_1^{pq}}{c} \frac{d}{dt} J_n(\tau_{mn}^{pq}) + I_2^{pq} J_n(\tau_{mn}^{pq}) \right] \end{aligned} \tag{78}$$

where I_1^{pq} and I_2^{pq} are given in (45). Substituting (76) and (78) into (38), we obtain

$$\sum_{n=1}^{N} \left[c_{mn} J_n(t) - \sum_{p,q} \left\{ \frac{I_1^{pq}}{c} \frac{d}{dt} J_n(\tau_{mn}^{pq}) + I_2^{pq} J_N(\tau_{mn}^{pq}) \right\} \right] = V_m^H(t) \tag{79}$$

where $V_m^H(t)$ is given by (47). Substituting the expansion (68) and (69) into (79) and taking the temporal testing with $\phi_i(st)$, we obtain

$$\begin{aligned} \sum_{n=1}^{N} \Bigg[c_{mn} \sum_{j=0}^{\infty} J_{n,j} \delta_{ij} - \sum_{p,q} \sum_{j=0}^{\infty} \Bigg\{ \left(\frac{s}{2} \frac{I_1^{pq}}{c} + I_2^{pq} \right) J_{n,j} + s \frac{I_1^{pq}}{c} \sum_{k=0}^{j-1} J_{n,k} \Bigg\} \\ \cdot I_{ij} \left(s \frac{R_{mn}^{pq}}{c} \right) \Bigg] = V_{m,i}^H \end{aligned} \tag{80}$$

where I_{ij} is given in (27) and $V_{m,i}^H$ is given in (49). Because $I_{ij} = 0$ when $j > 1$ from (A15), we can write the upper limit for the summation as i instead of ∞ in (80). In this result, moving the terms including $J_{n,j}$, which is known for $j < i$, to the right-hand side, we obtain

$$\begin{aligned}\sum_{n=1}^{N}\left\{c_{mn} - \sum_{p,q}\left(\frac{s}{2}\frac{I_1^{pq}}{c} + I_2^{pq}\right) I_{ii}\left(s\frac{R_{mn}^{pq}}{c}\right)\right\} J_{n,i} \\ = V_{m,i}^H + \sum_{n=1}^{N}\sum_{p,q}\left(\frac{s}{2}\frac{I_1^{pq}}{c} + I_2^{pq}\right)\sum_{j=0}^{i-1} J_{n,j} I_{ij}\left(s\frac{R_{mn}^{pq}}{c}\right) \\ + \sum_{n=1}^{N}\sum_{p,q} s\frac{I_1^{pq}}{c}\sum_{j=0}^{i}\sum_{k=0}^{j-1} J_{n,k} I_{ij}\left(s\frac{R_{mn}^{pq}}{c}\right) \end{aligned} \tag{81}$$

Rewriting (81) in a simple form, we obtain

$$\sum_{n=1}^{N} \alpha_{mn}^H J_{n,i} = V_{m,i}^H + P_{m,i}^H \tag{82}$$

where

$$\alpha_{mn}^H = c_{mn} - \sum_{p,q}\left(\frac{s}{2}\frac{I_1^{pq}}{c} + I_2^{pq}\right)\exp\left(-s\frac{R_{mn}^{pq}}{2c}\right) \tag{83}$$

$$\begin{aligned} P_{m,i}^H = \sum_{n=1}^{N}\sum_{p,q}\Bigg[\left(\frac{s}{2}\frac{I_1^{pq}}{c} + I_2^{pq}\right)\sum_{j=0}^{i-1} J_{n,j} I_{ij}\left(s\frac{R_{rm}^{pq}}{c}\right) \\ + s\frac{I_1^{pq}}{c}\sum_{j=0}^{i}\sum_{k=0}^{j-1} J_{n,k} I_{ij}\left(s\frac{R_{mn}^{pq}}{c}\right)\Bigg]. \end{aligned} \tag{84}$$

We can also write (82) in a matrix form as

$$\left[\alpha_{mn}^H\right]\left[J_{n,i}\right] = \left[\gamma_{m,i}^H\right] \tag{85}$$

where $\gamma_{m,i}^H = V_{m,i}^H + P_{m,i}^H$ and $i = 0, 1, \ldots, \infty$.

3.3. TD-CFIE

The matrix equation of the alternative TD-CFIE is obtained by combining (75) and (85), which results in

$$\left[\alpha_{mn}\right]\left[J_{n,i}\right] = \left[\gamma_{m,i}\right] \tag{86}$$

where the expressions of α_{mn} and $\gamma_{m,i}$ are similar to (57) and (58).

3.4. Current and Far Field

By solving (86) by a marching-on in degree algorithm with M temporal basis functions, we can obtain the current coefficient directly, which is given from (68) as

$$J_n(t) = \sum_{j=0}^{M-1} J_{n,j}\phi_j(st). \tag{87}$$

The far field expression is obtained using a similar procedure described in Section 2.4. Substituting (3) and (8) into (60) with (7), the far field is given as

$$\mathbf{E}^s(\mathbf{r},t) \approx -\frac{\mu}{8\pi}\sum_{n=1}^{N} l_n \sum_q \boldsymbol{\rho}_n^{cq}\frac{d}{dt}J_n(\tau_n^q) \tag{88}$$

where

$$\frac{d}{dt}J_n(\tau_n^q) = s\sum_{j=0}^{M-1}\left(\frac{1}{2}J_{n,j} + \sum_{k=0}^{j-1} J_{n,k}\right)\phi_j(s\tau_n^q). \tag{89}$$

4. NUMERICAL EXAMPLES

In this section, we present the numerical results for three representative 3-D closed conducting scatterers, viz. a sphere, a cube, and a cylinder, as shown in Fig. 1. The arrows on the scatterer surface indicate the location and direction of the current to be observed in Fig. 1. Fig. 1(a) shows a conducting sphere of radius 0.5 m centered at the origin. The first resonant frequency of this sphere occurs at 262 MHz. There are twelve and twenty-four divisions along the θ and ϕ directions with equally angular intervals. This results in a total of 528 patches and 792 common edges. The conducting cube, 1 m on a side, centered about the origin is shown in Fig. 1(b). The first resonant frequency of this cube is at 212 MHz. There are eight divisions along the x, y, and z directions, respectively. This represents a total of 768 patches and 1,152 common edges. Fig. 1(c) shows a conducting cylinder with a radius of 0.5 m and height of 1 m, centered at the origin. The first resonant frequency of this cylinder is at 230 MHz. We subdivide the cylinder into four, twenty-four, and eight divisions along r, ϕ, and z directions, respectively. This represents a total of 720 patches with 1,080 common edges. The scatterers are illuminated by a Gaussian

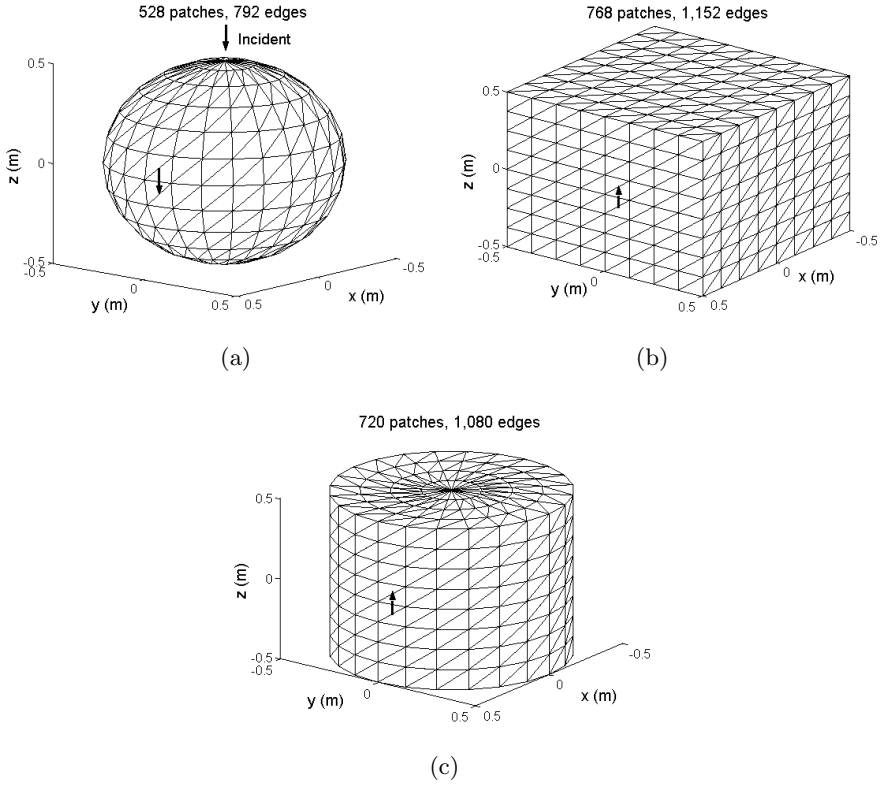

(a) (b)

(c)

Figure 1. Triangulation of conducting objects. (a) sphere. (b) cube. (c) cylinder.

plane wave, in which the electric and magnetic fields are given by

$$\mathbf{E}^i(\mathbf{r},t) = \mathbf{E}_0 \frac{4}{\sqrt{\pi}T} e^{-\gamma^2} \tag{90}$$

$$\mathbf{H}^i(\mathbf{r},t) = \frac{1}{\eta}\hat{\mathbf{k}} \times \mathbf{E}^i(\mathbf{r},t) \tag{91}$$

$$\gamma = \frac{4}{T}(ct - ct_0 - \mathbf{r}\cdot\hat{\mathbf{k}}) \tag{92}$$

where $\hat{\mathbf{k}}$ is the unit vector in the direction of the wave propagation, T is the pulse width of the Gaussian impulse, and t_0 is a time delay which represents the time at which the pulse peaks at the origin. In this work, the field is incident from $\phi = 0^\circ$ and $\theta = 0^\circ$ with $\hat{\mathbf{k}} = -\hat{\mathbf{z}}$, where this direction is displayed by an arrow above the top of the sphere in Fig. 1(a), and $\mathbf{E}_0 = \hat{\mathbf{x}}$. First, in the numerical computation,

we use a Gaussian pulse of $T = 8\,\text{lm}$ and $ct_0 = 12\,\text{lm}$. (The unit 'lm' denotes a light meter. A light meter is the length of time taken by the electromagnetic wave to travel 1 m in the free space.) This pulse has a frequency spectrum of 125 MHz, so the internal resonance effects are excluded for the structures shown in Fig. 1. Next, we use a Gaussian pulse of $T = 2\,\text{lm}$ and $ct_0 = 3\,\text{lm}$. This pulse has a frequency spectrum of 500 MHz, which encompasses several internal resonant frequencies of the structures shown in Fig. 1. The numerical results to be shown are transient currents on the surface and θ- (or x-) components of normalized far fields computed by EFIE, MFIE, and CFIE formulations. These far scattered fields from the structures are obtained along the backward direction, and hence represent the back-scattered fields. We also present the monostatic radar cross section (RCS) by considering both θ- and ϕ-components of the far fields in the decibel scale to represent the solutions in detail. All the numerical solutions have been computed using the methods presented, and have been compared with the inverse discrete Fourier transform (IDFT) of solutions obtained in the frequency-domain. We also compare the transient currents with the MOT solutions using the method in [2] for the resonant problems. In addition, far field solutions for the sphere are compared with the Mie series solutions. We set $s = 10^9$ and $M = 80$, which is sufficient to get accurate solutions. In all legends of the figures to be shown, the number '1' and '2' denote results computed by the formulation in Section 2 and the alternative formulation in Section 3, respectively.

4.1. Spectrum in the Non-Resonance Region

When the spectrum of the incident field excludes the resonance region, then for the non-resonance cases, we use an incident Gaussian pulse of $T = 8\,\text{lm}$. The purpose of this computation is to check the accuracy and validity of the TD-EFIE and TD-MFIE formulations excluding the resonance effects. As a first example, we consider the sphere of Fig. 1(a). Fig. 2 shows the transient response for the θ-directed current on the sphere computed by the TD-EFIE and compares them with an IDFT solution of the frequency-domain electric field integral equation (FD-EFIE). We can see that the solutions of the two described TD-EFIE methods are stable and the agreement with the IDFT solution is very good. Fig. 3 compares the transient field response of the two presented TD-EFIE methods along with the Mie series solution and the IDFT of the FD-EFIE solution for the normalized far scattered field and the monostatic RCS. All the four solutions agree well as is evident from the figures. Fig. 4 shows the transient response for the θ-directed current on the sphere computed by the TD-MFIE and compares them

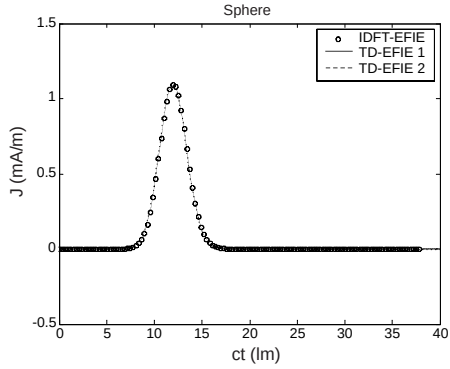

Figure 2. Transient current response on the sphere computed by EFIE with $T = 8\,\mathrm{lm}$.

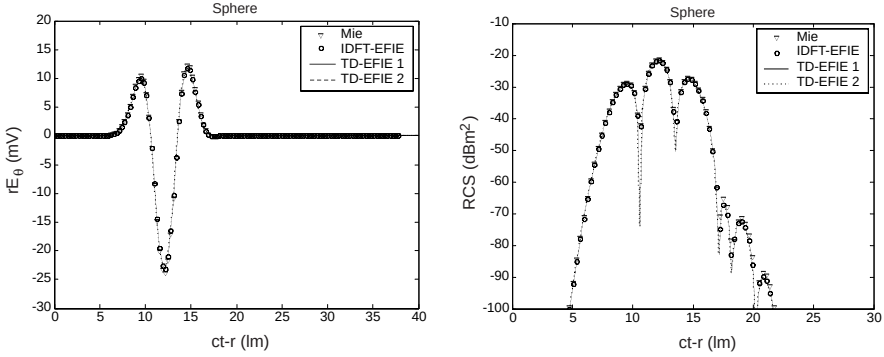

(a) (b)

Figure 3. Transient field response from the sphere computed by EFIE with $T = 8\,\mathrm{lm}$. (a) Far field. (b) RCS.

with the IDFT solution of the frequency-domain magnetic field integral equation (FD-MFIE). We can see that solutions of the presented two TD-MFIE methods are stable and the agreement with the IDFT solution is very good. Fig. 5 compares the transient response of the two presented TD-MFIE methods with the Mie series solution and the IDFT of the FD-MFIE solution for the normalized far scattered field and the monostatic RCS of the sphere. All the four solutions agree well as is evident from the figures. Fig. 6 shows the transient response for the θ-directed current on the sphere computed by the TD-CFIE and compares them with the IDFT solution of the frequency-domain combined field integral equation (FD-CFIE). We can see that

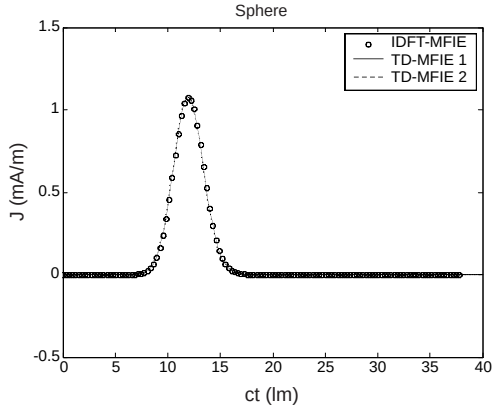

Figure 4. Transient current response on the sphere computed by MFIE with $T = 8\,\mathrm{lm}$.

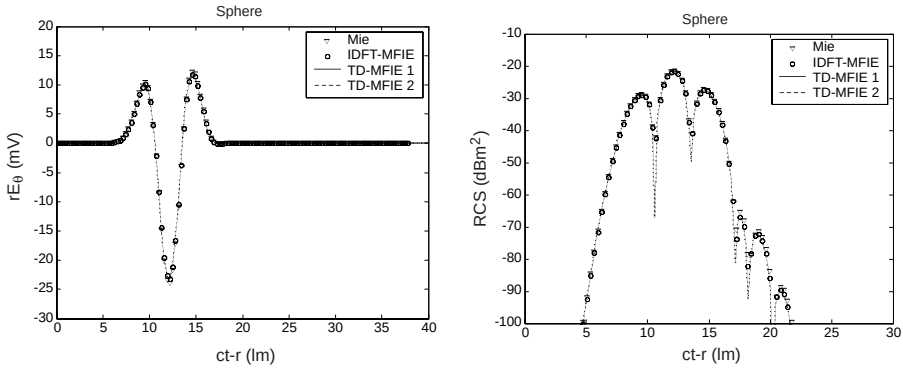

(a) (b)

Figure 5. Transient field response from the sphere computed by MFIE with $T = 8\,\mathrm{lm}$. (a) Far field. (b) RCS.

the solutions obtained from the two presented TD-CFIE methods are stable and the agreement with the IDFT solution is very good. Fig. 7 compares the transient field response of the two presented TD-CFIE methods along with the Mie series solution and the IDFT of the FD-CFIE solution for the normalized far scattered field and the monostatic RCS from the sphere. All the four solutions agree well as is evident from the figure.

As a second example, we consider the cube of Fig. 1(b). Fig. 8 shows the transient response for the z-directed current on the cube computed by the TD-EFIE and compares them with IDFT solution

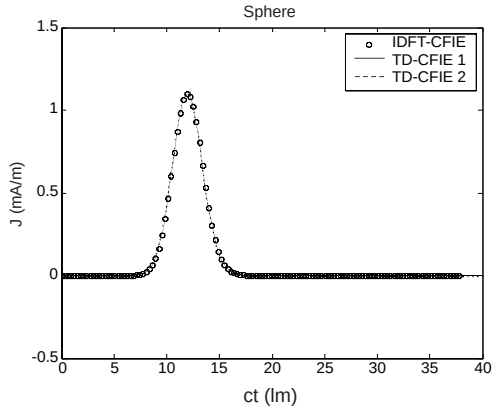

Figure 6. Transient current response on the sphere computed by CFIE with $T = 8\,\mathrm{lm}$.

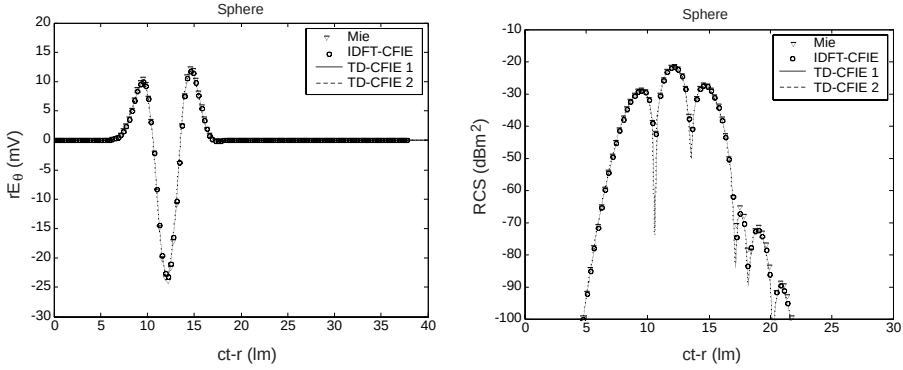

Figure 7. Transient field response from the sphere computed by CFIE with $T = 8\,\mathrm{lm}$. (a) Far field. (b) RCS.

of the FD-EFIE. We can see that the solutions for the two presented TD-EFIE methods are stable and are in agreement with the IDFT solution. Fig. 9 compares the transient electric field response of the two presented TD-EFIE methods with the IDFT of the FD-EFIE solution for the normalized far scattered field and the monostatic RCS from the cube. All the three solutions agree well as is evident from this figure. Fig. 10 shows the transient response for the z-directed current on the cube computed by the TD-MFIE and compares them with IDFT solution of the FD-MFIE. We can see that solutions of the

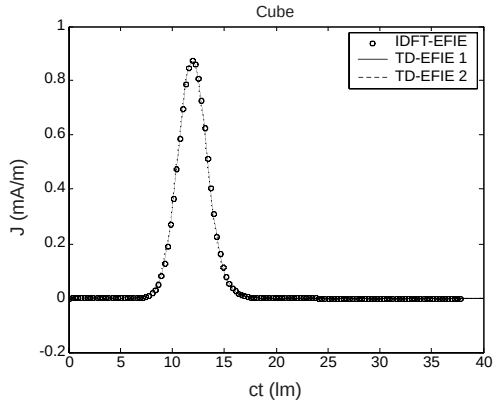

Figure 8. Transient current response on the cube computed by EFIE with $T = 8\,\mathrm{lm}$.

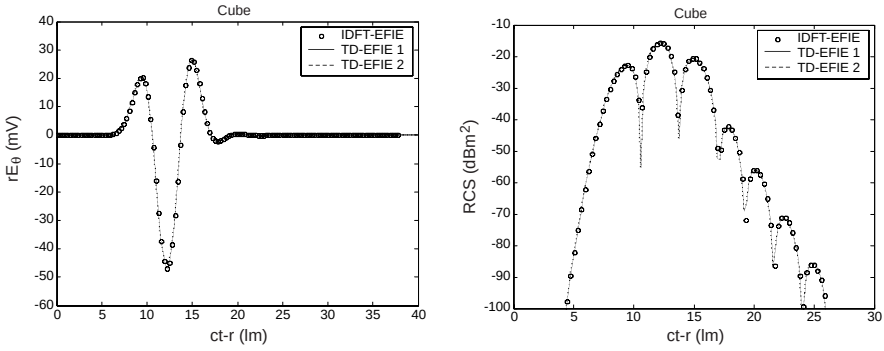

(a) (b)

Figure 9. Transient field response from the cube computed by EFIE with $T = 8\,\mathrm{lm}$. (a) Far field. (b) RCS.

two presented TD-MFIE methods are stable and the agreement with the IDFT solution is very good. Fig. 11 compares the transient field response of the two presented TD-MFIE methods with the IDFT of the FD-MFIE solution for the normalized far scattered field and the monostatic RCS from the cube. All the three solutions agree well as is evident from the figure. Fig. 12 shows the transient response for the z-directed current on the cube computed by the TD-CFIE and compares them with the IDFT solution of the FD-CFIE. We can see that the solutions obtained from the two presented TD-CFIE methods are stable and the agreement with the IDFT solution is very good.

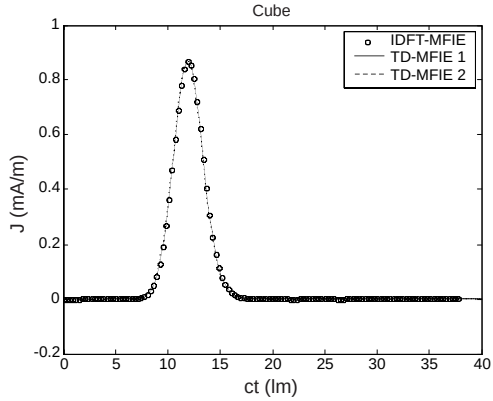

Figure 10. Transient current response on the cube computed by MFIE with $T = 8\,\mathrm{lm}$.

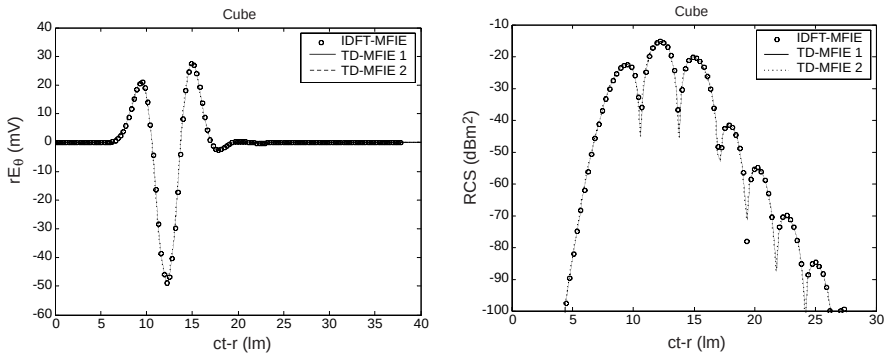

(a) (b)

Figure 11. Transient field response from the cube computed by MFIE with $T = 8\,\mathrm{lm}$. (a) Far field. (b) RCS.

Fig. 13 compares the transient field response of the two presented TD-CFIE methods with the IDFT of the FD-CFIE solution for the normalized far scattered field and the monostatic RCS from the cube. All the three solutions agree well as is evident from the figure.

As a third example, we consider the cylinder in Fig. 1(c). Fig. 14 shows the transient response for the z-directed current on the cylinder computed by the TD-EFIE and compares them with the IDFT solution of the FD-EFIE. We can see that solutions of the two presented TD-EFIE methods are stable and the agreement with the IDFT solution is very good. Fig. 15 compares the transient field response of two

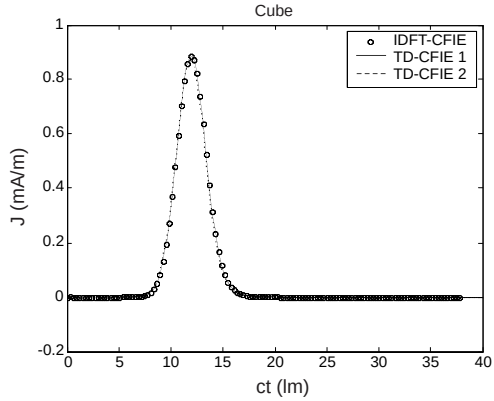

Figure 12. Transient current response on the cube computed by CFIE with $T = 8\,\mathrm{lm}$.

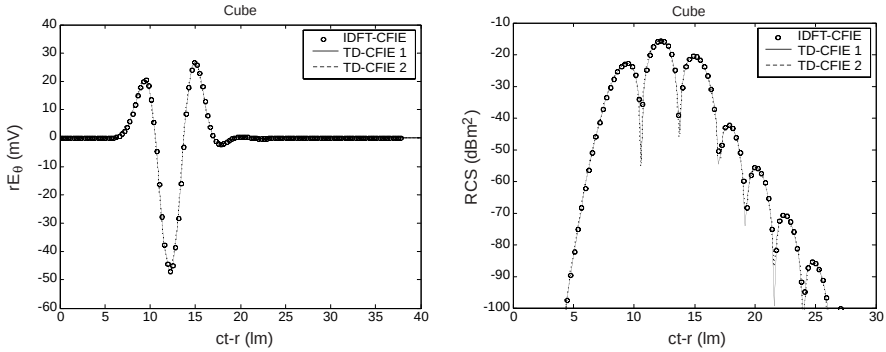

(a) (b)

Figure 13. Transient field response from the cube computed by CFIE with $T = 8\,\mathrm{lm}$. (a) Far field. (b) RCS.

presented TD-EFIE methods with the IDFT of the FD-EFIE solution for the normalized far scattered field and monostatic RCS from the cylinder. All the three solutions agree well as is evident from the figure. Fig. 16 shows the transient response for the z-directed current on the cylinder computed by the TD-MFIE and compares them with the IDFT solution of the FD-MFIE. We can see that solutions of the two presented TD-MFIE methods are stable and the agreement with the IDFT solution is very good. Fig. 17 compares the transient field response of the two presented TD-MFIE methods with the IDFT of the FD-MFIE solution for the normalized far scattered field and the

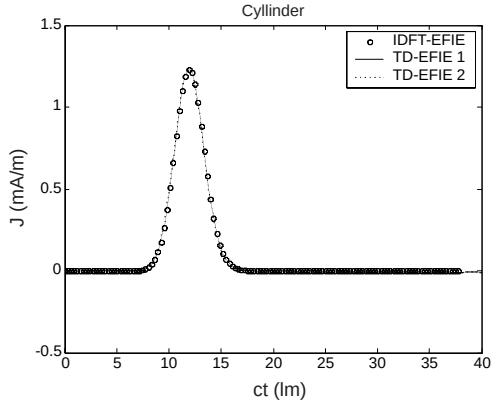

Figure 14. Transient current response on the cylinder computed by EFIE with $T = 8\,\mathrm{lm}$.

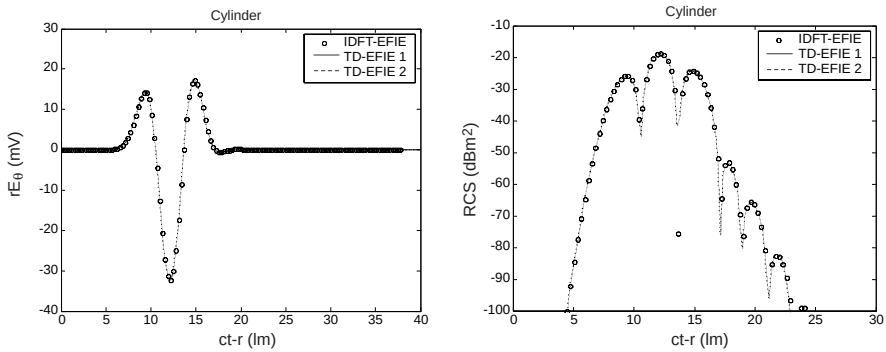

(a) (b)

Figure 15. Transient field response from the cylinder computed by EFIE with $T = 8\,\mathrm{lm}$. (a) Far field. (b) RCS.

monostatic RCS from the cylinder. All the three solutions agree well as is evident from the figure. Fig. 18 shows the transient response for the z-directed current on the cylinder computed by the TD-CFIE and compares them with the IDFT solution of the FD-CFIE. We can see that solutions of the two presented TD-CFIE methods are stable and the agreement with the IDFT solution is very good. Fig. 19 compares the transient field response of the two presented TD-CFIE methods with the IDFT of the FD-CFIE solution for the normalized far scattered field and the monostatic RCS from the cylinder. All the three solutions agree well as is evident from the figure.

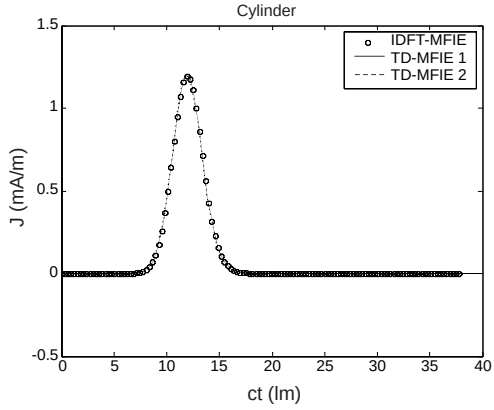

Figure 16. Transient current response on the cylinder computed by MFIE with $T = 8\,\mathrm{lm}$.

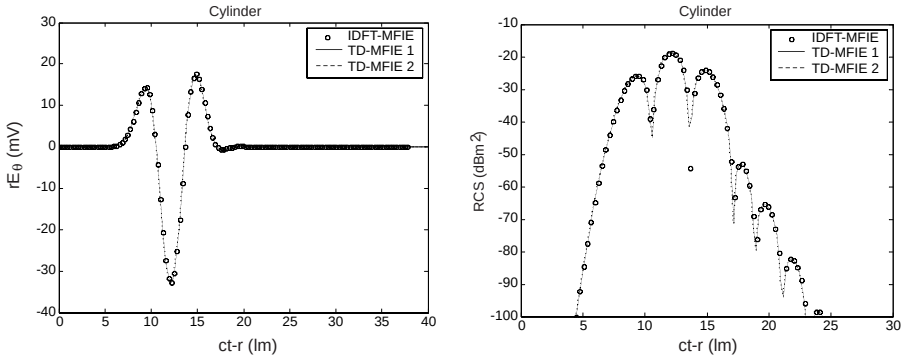

(a) (b)

Figure 17. Transient field response from the cylinder computed by MFIE with $T = 8\,\mathrm{lm}$. (a) Far field. (b) RCS.

4.2. Responses Due to Wide-Band Incident Waveform

When the bandwidth of the incident signal is large, it can induce numerical internal resonances for the structures. In this case, we use a Gaussian pulse with $T = 2\,\mathrm{lm}$, whose spectrum overlaps over several internal resonant frequencies of the scattering structures. As a first example, we consider the sphere of Fig. 1(a). The time step in the MOT computation is chosen such that $c\Delta t = 4R_{\min}$ in order to generate the implicit solution, where $R_{\min}$ represents the minimum distance between any two distinct patch centers and $R_{\min}$ is 2.23 cm in the

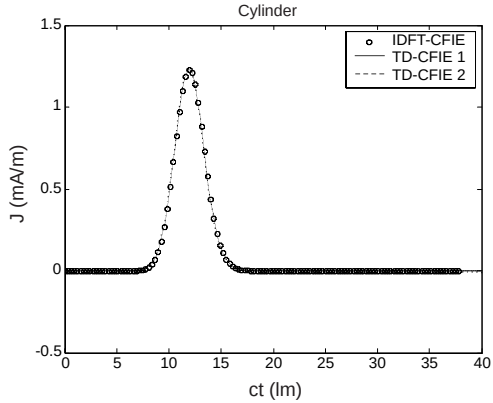

Figure 18. Transient current response on the cylinder computed by CFIE with $T = 8\,\mathrm{lm}$.

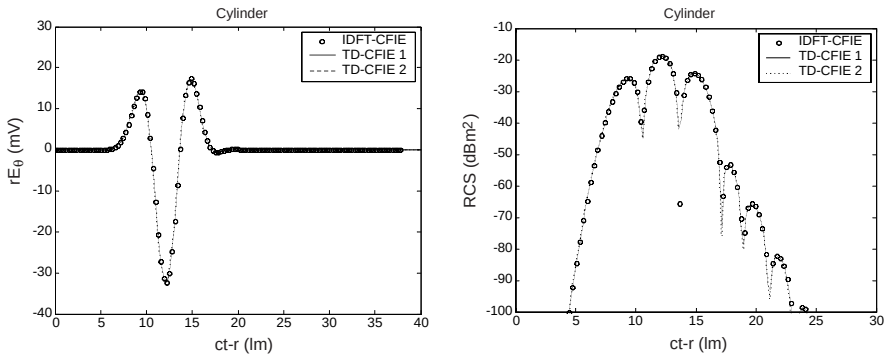

(a) (b)

Figure 19. Transient field response from the cylinder computed by CFIE with $T = 8\,\mathrm{lm}$. (a) Far field. (b) RCS.

sphere model. Fig. 20 shows the transient response for the θ-directed current on the sphere computed by the TD-EFIE and compares them with the IDFT solution of the FD-EFIE and the MOT solution of the TD-EFIE. We can see that solutions of the two presented TD-EFIE methods are stable and are in agreement with the IDFT and MOT solutions. The agreement is very good except a late-time oscillation of the MOT solution appears. Fig. 21 compares the transient field response of the two presented TD-EFIE methods with the Mie series solution and the IDFT of the FD-EFIE solution for the normalized far scattered field and the monostatic RCS from the sphere. All the four

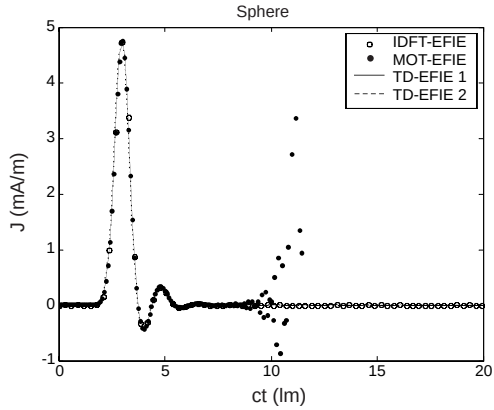

Figure 20. Transient current response on the sphere computed by EFIE with $T = 2\,\mathrm{lm}$.

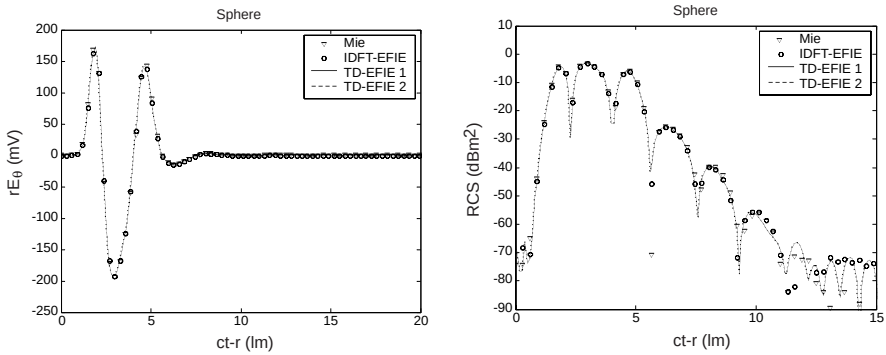

(a) (b)

Figure 21. Transient field response from the sphere computed by EFIE with $T = 2\,\mathrm{lm}$. (a) Far field. (b) RCS.

solutions agree well as is evident from the figure. Fig. 22 shows the transient response for the θ-directed current on the sphere computed by the TD-MFIE and compares them with the IDFT solution of the FD-MFIE and the MOT solution of the TD-MFIE. We can see that solutions of the two presented TD-MFIE methods are stable and the agreement with the IDFT is very good, while the MOT solution is not accurate as it displays slowly varying oscillations. Fig. 23 compares the transient field response of the two presented TD-MFIE methods along with the Mie series solution and the IDFT of the FD-MFIE solution for the normalized far scattered field and the monostatic RCS from

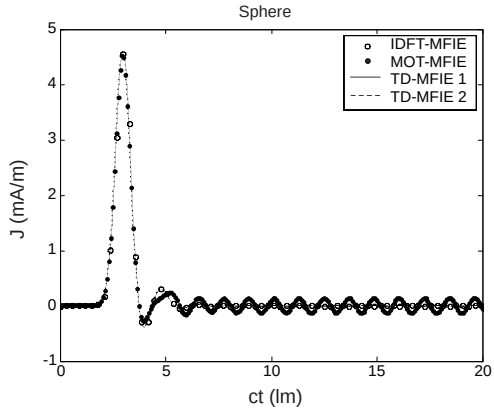

Figure 22. Transient current response on the sphere computed by MFIE with $T = 2\,\mathrm{lm}$.

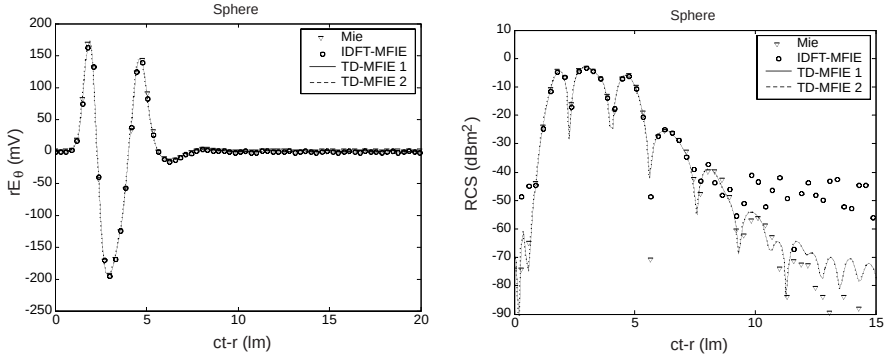

(a) (b)

Figure 23. Transient field response from the sphere computed by MFIE with $T = 2\,\mathrm{lm}$. (a) Far field. (b) RCS.

the sphere. All the four solutions show a good agreement for the far field in Fig. 23(a). In Fig. 23(b), however, we note that the IDFT solution of the FD-MFIE is different from the Mie series solution in the lower values of the RCS. Fig. 24 shows the transient response for the θ-directed current on the sphere computed by the TD-CFIE and compares them with IDFT solution of the FD-CFIE and the MOT solution of the TD-CFIE. We can see that the solutions for the two presented TD-CFIE methods are stable and the agreement with the IDFT and MOT solutions is good. Fig. 25 compares the transient field response of the two presented TD-CFIE methods along with the

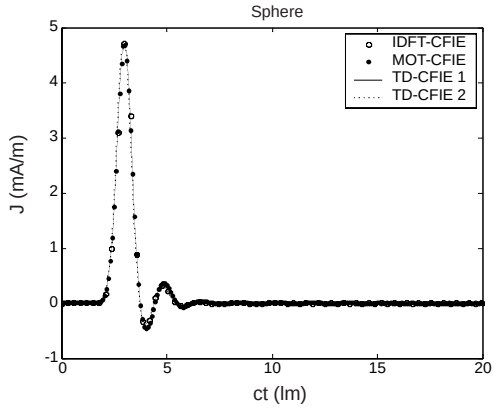

Figure 24. Transient current response on the sphere computed by CFIE with $T = 2\,\mathrm{lm}$.

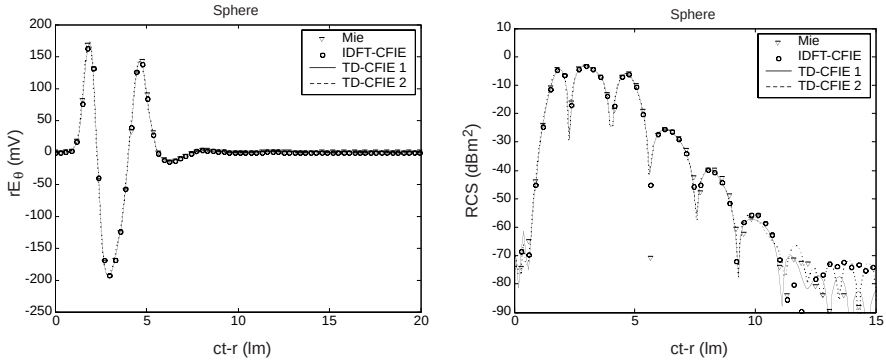

(a) (b)

Figure 25. Transient field response from the sphere computed by CFIE with $T = 2\,\mathrm{lm}$. (a) Far field. (b) RCS.

Mie series solution and the IDFT of the FD-CFIE solution for the normalized far scattered field and the monostatic RCS from the sphere. All the four solutions agree well as is evident from the figure. It is important to note that the TD-CFIE solutions are more accurate than those of the TD-EFIE and the TD-MFIE in the low values for the RCS.

As a second example, we consider the cube in Fig. 1(b). The time step in the MOT computation is chosen such that $c\Delta t = 2R_{\min}$ in order to generate the implicit solution, where $R_{\min}$ is 5.57 cm in the cube model. Fig. 26 shows the transient response for the z-directed

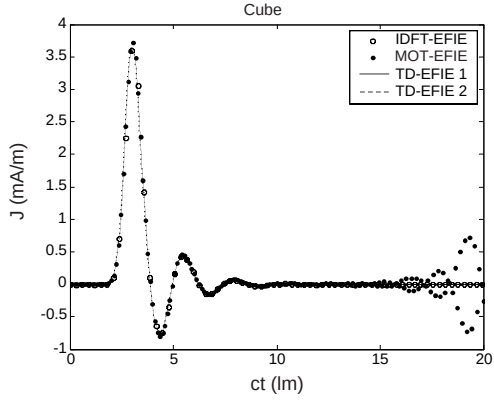

Figure 26. Transient current response on the cube computed by EFIE with $T = 2\,\mathrm{lm}$.

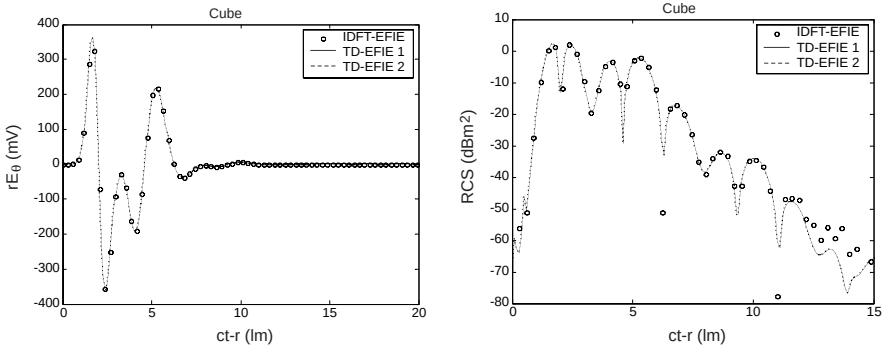

(a) (b)

Figure 27. Transient field response from the cube computed by EFIE with $T = 2\,\mathrm{lm}$. (a) Far field. (b) RCS.

current on the cube computed by the TD-EFIE and compares them with the IDFT solution of the FD-EFIE and the MOT solution of the TD-EFIE. We can see that solutions for the two presented TD-EFIE methods are stable and the agreement with the IDFT and MOT solutions is very good except for the late-time oscillations displayed by the MOT solution. Fig. 27 compares the transient field response of the two presented TD-EFIE methods along with the IDFT of the FD-EFIE solution for the normalized far scattered field and the monostatic RCS from the cube. All the three solutions agree well as is evident from the figure. Fig. 28 shows the transient response for the z-directed

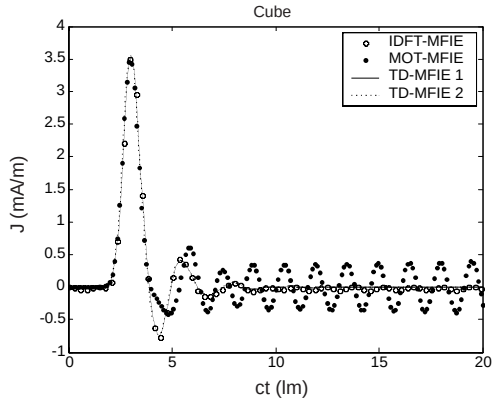

Figure 28. Transient current response on the cube computed by MFIE with $T = 2\,\mathrm{lm}$.

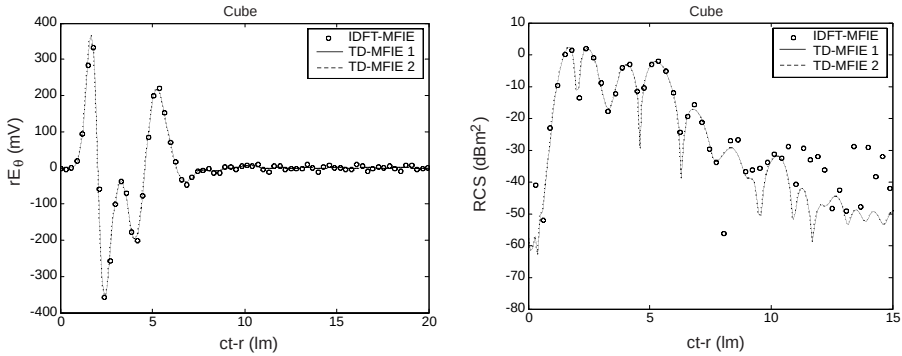

(a) (b)

Figure 29. Transient field response from the cube computed by MFIE with $T = 2\,\mathrm{lm}$. (a) Far field. (b) RCS.

current on the cube computed by the TD-MFIE and compares them with IDFT solution of the FD-MFIE and the MOT solution of the TD-MFIE. We can see that the solutions of the two presented TD-MFIE methods are stable and the agreement with the IDFT is good, while the MOT solution is not accurate with slowly varying oscillations. Fig. 29 compares the transient field response of the two presented TD-MFIE methods along with the IDFT of the FD-MFIE solution for the normalized far scattered field and the monostatic RCS from the cube. All the three solutions show a good agreement for the far field with a small fluctuation of the IDFT solution as in Fig. 29(a). However,

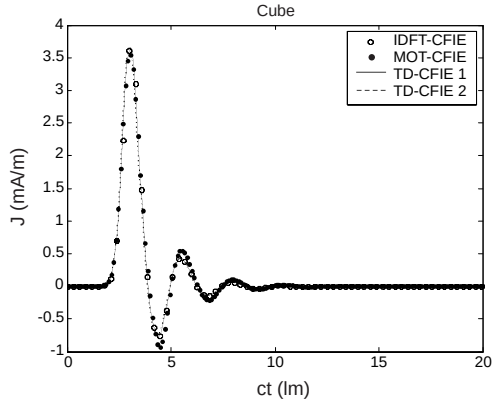

Figure 30. Transient current response on the cube computed by CFIE with $T = 2\,\mathrm{lm}$.

we note that there is a difference between the TD-MFIE solutions and the IDFT solution of FD-MFIE in the low level of the RCS as shown in Fig. 29(b). Fig. 30 shows the transient response for the z-directed current on the cube computed by the TD-CFIE and compares them with IDFT solution of the FD-CFIE and the MOT solution of the TD-CFIE. We can see that the solutions of the two presented TD-CFIE methods are stable and the agreement with the IDFT solution is very good, while the MOT solution is stable but not accurate. The MOT solution has small differences from the other solutions in the second and third peaks in Fig. 30. This is due to the instabilities of the TD-MFIE as shown in Fig. 28. When using the explicit MOT scheme along with the TD-CFIE, the solution become more accurate, and this has been pointed out in [2]. Fig. 31 compares the transient field response of the two presented TD-CFIE methods along with the IDFT of the FD-CFIE solution for the normalized far scattered field and the monostatic RCS for the cube. All the three solutions show a good agreement for the far field in Fig. 31(a). It is important to note that solutions for the TD-CFIE show better agreement with the IDFT solution than those of TD-EFIE and TD-MFIE in the low levels of the RCS.

As a third example, we consider the cylinder in Fig. 1(c). The time step in the MOT computation is chosen such that $c\Delta t = 4R_{\min}$ in order to generate the implicit solution, where $R_{\min}$ is 2.15 cm in the cylinder model. Fig. 32 shows the transient response for the z-directed current on the cylinder computed by the TD-EFIE and compares them with the IDFT solution of the FD-EFIE and the MOT solution of the TD-EFIE. We can see that solutions of the two presented TD-EFIE methods are stable and the agreement with the IDFT and MOT

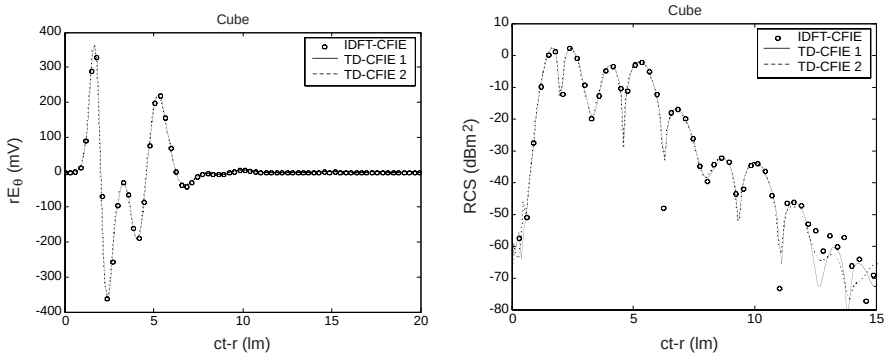

(a) (b)

Figure 31. Transient field response from the cube computed by CFIE with $T = 2\,\mathrm{lm}$. (a) Far field. (b) RCS.

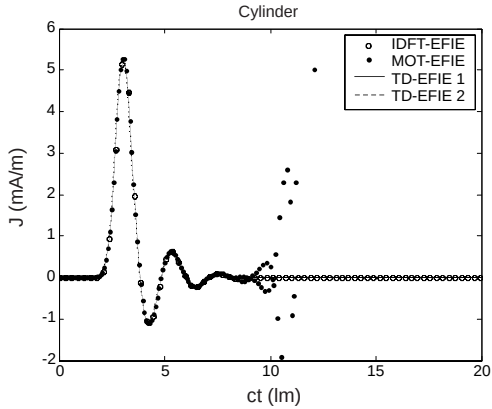

Figure 32. Transient current response on the cylinder computed by EFIE with $T = 2\,\mathrm{lm}$.

solutions is very good except for the late-time oscillations displayed by the MOT solution. Fig. 33 compares the transient field response of two TD-EFIE methods along with the IDFT of the FD-EFIE solution for the normalized far scattered field and the monostatic RCS of the cylinder. All the three solutions agree well as is evident from the figure. Fig. 34 shows the transient response for the z-directed current on the cylinder computed by the TD-MFIE and compares them with the IDFT solution of the FD-MFIE and the MOT solution of the TD-MFIE. We can see that solutions of the two presented TD-MFIE methods are stable and the agreement with IDFT is very good, while

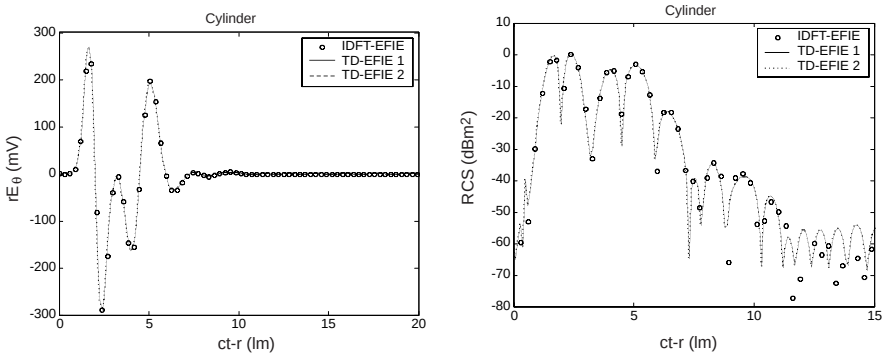

(a) (b)

Figure 33. Transient field response from the cylinder computed by EFIE with $T = 2\,\mathrm{lm}$. (a) Far field. (b) RCS.

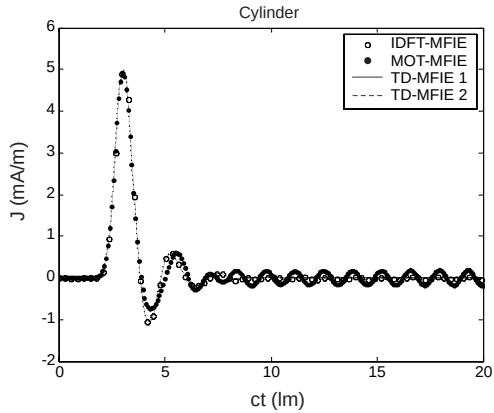

Figure 34. Transient current response on the cylinder computed by MFIE with $T = 2\,\mathrm{lm}$.

the MOT solution is not accurate with slowly varying oscillation. Fig. 35 compares the transient field response of the two presented TD-MFIE methods along with the IDFT of the FD-MFIE solution for the normalized far scattered field and the monostatic RCS from the cylinder. All the three solutions show a good agreement for the far field with a small fluctuation of the IDFT solution in Fig. 35(a). Also, we note that there is a difference between the TD-MFIE solutions and the IDFT solution of FD-MFIE in the low level of the RCS in Fig. 35(b). Fig. 36 shows the transient response for the z-directed current on the cylinder computed by the TD-CFIE and compares them with the IDFT

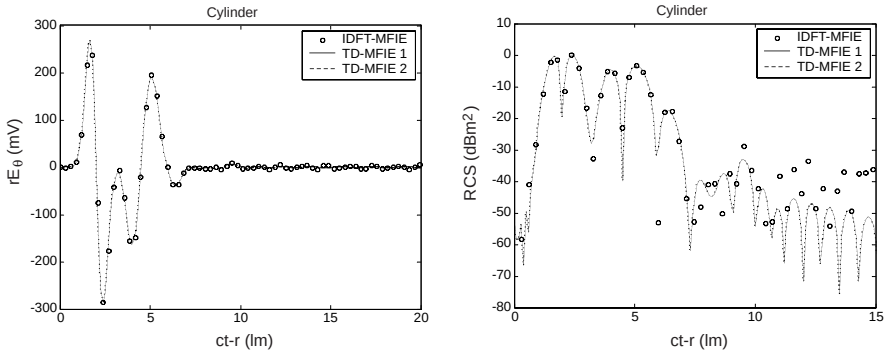

(a) (b)

Figure 35. Transient field response from the cylinder computed by MFIE with $T = 2\,\mathrm{lm}$. (a) Far field. (b) RCS.

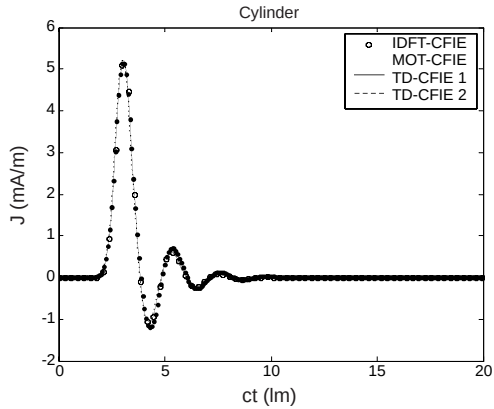

Figure 36. Transient current response on the cylinder computed by CFIE with $T = 2\,\mathrm{lm}$.

solution of the FD-CFIE and the MOT solution of the TD-CFIE. We can see that solutions for the two presented TD-CFIE methods are stable and the agreement with the IDFT solution is very good, while the MOT solution is stable but has a small difference in the second and third peaks in Fig. 36. Fig. 37 compares the transient field response of the two presented TD-CFIE methods with the IDFT of the FD-CFIE solution for the normalized far scattered field and the monostatic RCS from the cylinder. All the three solutions show a good agreement for the far field in Fig. 37(a). However, we note that solutions of the two presented TD-CFIE methods show better agreement with the IDFT

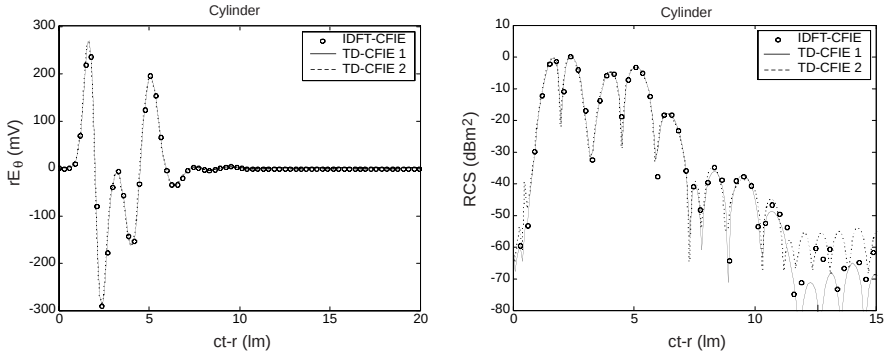

(a) (b)

Figure 37. Transient field response from the cylinder computed by CFIE with $T = 2\,\mathrm{lm}$. (a) Far field. (b) RCS.

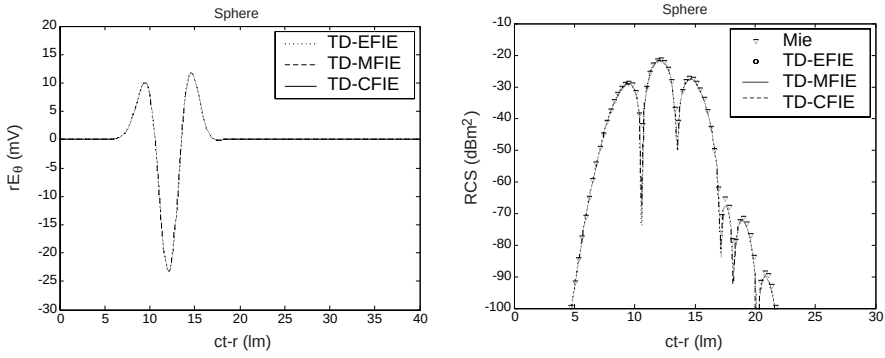

(a) (b)

Figure 38. Comparison of solutions for the sphere computed by EFIE, MFIE, and CFIE with $T = 8\,\mathrm{lm}$. (a) Far field. (b) RCS.

solution than those of TD-EFIE and TD-MFIE in the regions of low values of the RCS.

Finally, we compare far field solutions computed by TD-EFIE, TD-MFIE, and TD-CFIE for the sphere, which has an analytic solution, in the same figure, simultaneously. Fig. 38 shows solutions of the far field and the RCS when the Gaussian pulse with $T = 8\,\mathrm{lm}$ is used. In this example, because of exclusion of the internal resonance frequencies in the excitation, the agreement between the solutions is excellent. The RCS also shows good agreement with the Mie series solution in Fig. 38(b). Fig. 39 shows the results when the Gaussian

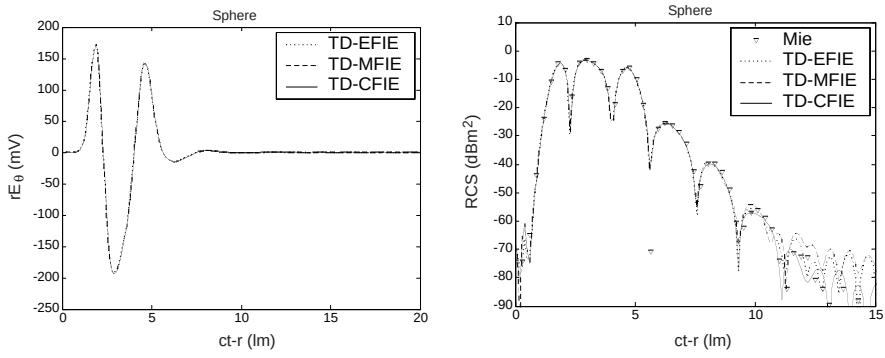

(a) (b)

Figure 39. Comparison of solutions for the sphere computed by EFIE, MFIE, and CFIE with $T = 2\,\mathrm{lm}$. (a) Far field. (b) RCS.

pulse width is small, i.e., $T = 2\,\mathrm{lm}$. Even though this excitation covers the internal resonant frequencies, solutions of the TD-EFIE and the TD-MFIE agree well with TD-CFIE in Fig. 39(a). All the three solutions agree well with the Mie series solution except in the extremely low values of the RCS as shown in Fig. 39(b).

5. CONCLUSION

We presented two methods to solve the time-domain integral equation for arbitrarily shaped 3-D conducting structures. To apply a MoM procedure, we used triangular patch functions as spatial basis and testing functions. We introduced a temporal basis function set derived from Laguerre polynomials. The advantage of the proposed methods is to guarantee the late time stability. With the representation of the derivative of the transient coefficient in an analytic form, the temporal derivative in the integral equations can be treated analytically. Transient electric current and the far field obtained by the two presented methods are accurate and stable. The agreement between the solutions obtained using the two proposed methods and the IDFT of the frequency domain is excellent.

APPENDIX A.

Consider the set of functions [18],

$$L_j(t) = \frac{e^t}{j!}\frac{d^j}{dt^j}(t^j e^{-t}), \quad 0 \le t < \infty, \quad j = 0, 1, 2, \ldots. \tag{A1}$$

These are the Laguerre functions of degree j. They are causal, i.e., they are defined for $t \geq 0$. They can be computed in a stable fashion recursively through

$$L_0(t) = 1 \tag{A2}$$

$$L_1(t) = 1 - t \tag{A3}$$

$$L_j(t) = \frac{1}{j}\big[(2j-1-t)L_{j-1}(t) - (j-1)L_{j-2}(t)\big], \quad j \geq 2. \tag{A4}$$

The Laguerre functions are orthogonal as

$$\int_0^\infty e^{-t} L_i(t) L_j(t) dt = \delta_{ij} = \begin{cases} 1, & i = j \\ 0, & i \neq j \end{cases}. \tag{A5}$$

A causal electromagnetic response function $f(t)$ at a particular location in space for $t \geq 0$ can be expanded using (22) as

$$f(t) = \sum_{j=0}^{\infty} f_j \phi_j(t). \tag{A6}$$

By multiplying the function $f(t)$ with $\phi_i(t)$ and integrating from zero to infinity, which we call a Laguerre transform here, we get

$$\int_0^\infty \phi_i(t) f(t) dt = f_i. \tag{A7}$$

In obtaining (A7), the orthogonal relation (A5) has been used. Also, we can use the result of the Laguerre transform to obtain an analytic representation for the derivative of the function $f(t)$ as

$$\int_0^\infty \phi_i(t) \frac{d}{dt} f(t) dt = \frac{1}{2} f_i + \sum_{k=0}^{i-1} f_k \tag{A8}$$

where $f(0) = 0$ is assumed and $\phi_i(\infty) = 0$ is used. Using the relations (A6) and (A7), we can expand the derivative of the function $f(t)$ using (22) and (A8) as

$$\frac{d}{dt} f(t) = \sum_{j=0}^{\infty} \left(\frac{1}{2} f_j + \sum_{k=0}^{j-1} f_k \right) \phi_j(t). \tag{A9}$$

Similarly, the result for the second derivative of the function $f(t)$ is given as

$$\frac{d^2}{dt^2} f(t) = \sum_{j=0}^{\infty} \left[\left(\frac{1}{4} f_j + \sum_{k=0}^{j-1} (j-k) f_k \right) \right] \phi_j(t). \tag{A10}$$

Now, we consider the integral defined in (27). For the simplicity, we rewrite (27) as

$$I_{ij}(y) = \int_0^\infty \phi_i(x)\phi_j(x-y)dx. \tag{A11}$$

Through a change of variable as $z = x - y$ in (A11) and using (22), we have

$$I_{ij}(y) = e^{-y/2} \int_{-y}^\infty e^{-z} L_i(z+y) L_j(z) dz. \tag{A12}$$

Using the formula (8.971) and (8.974) in [19], we obtain

$$L_i(z+y) = \sum_{k=0}^{i} L_k(z)\big[L_{i-k}(y) - L_{i-k-1}(y)\big]. \tag{A13}$$

Substituting (A13) into (A12), we obtain

$$I_{ij}(y) = e^{-y/2} \sum_{k=0}^{i} \big[L_{i-k}(y) - L_{i-k-1}(y)\big] \int_{-y}^\infty e^{-z} L_k(z) L_j(z) dz. \tag{A14}$$

Because the Laguerre function in (A14) is defined for $z \geq 0$, the lower limit of the integral in (A14) may be changed from $-y$ to zero, and hence the integral can be computed easily by (A5). Finally, we have

$$I_{ij}(y) = \begin{cases} e^{-y/2}\big[L_{i-j}(y) - L_{i-j-1}(y)\big], & j \leq i \\ 0, & j > i \end{cases}. \tag{A15}$$

REFERENCES

1. Shankar, B., A. A. Ergin, K. Aygun, and E. Michielssen, "Analysis of transient electromagnetic scattering from closed surfaces using a combined field integral equation," *IEEE Trans. Antennas Propagat.*, Vol. 48, No. 7, 1064–1074, July 2000.
2. Jung, B. H. and T. K. Sarkar, "Time-domain CFIE for the analysis of transient scattering from arbitrarily shaped 3D conducting objects," *Microwave Opt. Technol. Lett.*, Vol. 34, No. 4, 289–296, Aug. 2002.
3. Rao, S. M., *Time Domain Electromagnetics*, Academic Press, 1999.

4. Rao, S. M. and D. R. Wilton, "Transient scattering by conducting surfaces of arbitrary shape," *IEEE Trans. Antennas Propagat.*, Vol. 39, No. 1, 56–61, Jan. 1991.
5. Vechinski, D. A. and S. M. Rao, "A stable procedure to calculate the transient scattering by conducting surfaces of arbitrary shape," *IEEE Trans. Antennas Propagat.*, Vol. 40, No. 6, 661–665, June 1992.
6. Rao, S. M. and T. K. Sarkar, "An alternative version of the time-domain electric field integral equation for arbitrarily shaped conductors," *IEEE Trans. Antennas Propagat.*, Vol. 41, No. 6, 831–834, June 1993.
7. Rao, S. M. and T. K. Sarkar, "An efficient method to evaluate the time-domain scattering from arbitrarily shaped conducting bodies," *Microwave Opt. Technol. Lett.*, Vol. 17, No. 5, 321–325, April 1998.
8. Sarkar, T. K., W. Lee, and S. M. Rao, "Analysis of transient scattering from composite arbitrarily shaped complex structures," *IEEE Trans. Antennas Propagat.*, Vol. 48, No. 10, 1625–1634, April 2000.
9. Jung, B. H. and T. K. Sarkar, "Time-domain electric-field integral equation with central finite difference," *Microwave Opt. Technol. Lett.*, Vol. 31, No. 6, 429–435, Dec. 2001.
10. Jung, B. H. and T. K. Sarkar, "An accurate and stable implicit solution for transient scattering and radiation from wire structures," *Microwave Opt. Technol. Lett.*, Vol. 34, No. 5, 354–359, Sept. 2002.
11. Jung, B. H. and T. K. Sarkar, "Transient scattering from three-dimensional conducting bodies by using magnetic field integral equation," *J. of Electromagn. Waves and Applicat.*, Vol. 16, No. 1, 111–128, Jan. 2002.
12. Sarkar, T. K. and J. Koh, "Generation of a wide-band electromagnetic response through a Laguerre expansion using early-time and low-frequency data," *IEEE Trans. Antennas Propagat.*, Vol. 50, No. 5, 1408–1416, May 2002.
13. Rao, S. M., D. R. Wilton, and A. W. Glisson, "Electromagnetic scattering by surfaces of arbitrary shape," *IEEE Trans. Antennas Propagat.*, Vol. 30, No. 3, 409–418, May 1982.
14. Wilton, D. R., S. M. Rao, A. W. Glisson, D. H. Schaubert, O. M. Al-Bundak, and C. M. Butler, "Potential integrals for uniform and linear source distributions on polygonal and polyhedral domains," *IEEE Trans. Antennas Propagat.*, Vol. 32, No. 3, 276–281, March 1984.

15. Rao, S. M., "Electromagnetic scattering and radiation of arbitrarily-shaped surfaces by triangular patch modeling," Ph.D. Dissertation, Univ. Mississippi, Aug. 1980.
16. Van Bladel, J., *Electromagnetic Fields*, Hemisphere Publishing Coporation, 1985.
17. Poggio, A. J. and E. K. Miller, "Integral equation solutions of three dimensional scattering problems," *Computer Techniques for Electromagnetics*, Pergamon Press, New York, 1973.
18. Poularikas, A. D., *The Transforms and Applications Handbook*, IEEE Press, 1996.
19. Gradshteyn, I. S. and I. M. Ryzhik, *Table of Integrals, Series, and Products*, Academic Press, New York, 1980.
20. Chung, Y. S., T. K. Sarkar, B. H. Jung, and J. Zhong, "Solution of time domain electric field integral equation using an unconditionally stable methodology," *IEEE Trans. Antennas Propagat.*, to be published.
21. Chung, Y. S, T. K. Sarkar, and B. H. Jung, "Solution of time domain magnetic field integral equation for arbitrarily closed conducting bodies using an unconditionally stable methodology," *Microwave Opt. Technol. Lett.*, to be published.
22. Chung, Y. S., T. K. Sarkar, and B. H. Jung, "An unconditionslly stable scheme for finite difference time domain (FDTD) method," *IEEE Trans. Microwave Theory and Tech.*, to be published.